Non-canonical apical constriction shapes emergent matrices in *C. elegans*

Sophie S. Katz[1] and Alison R. Frand[1]

[1]Department of Biological Chemistry

David Geffen School of Medicine

University of California, Los Angeles

Los Angeles, CA 90095

*To whom correspondence should be addressed: afrand@mednet.ucla.edu

Keywords: Actomyosin cytoskeleton, adherens junctions, epidermal morphogenesis, cuticle patterning, *C. elegans* molting cycle

SUMMARY

We describe a morphogenetic mechanism that integrates apical constriction with remodeling apical extracellular matrices. Therein, a pulse of anisotropic constriction generates transient epithelial protrusions coupled to an interim apical matrix, which then patterns long durable ridges on *C. elegans* cuticles.

ABSTRACT

Specialized epithelia produce intricate apical matrices by poorly defined mechanisms. To address this question, we studied the role of apical constriction in patterning the acellular cuticle of *C. elegans*. Knocking-down epidermal actin, non-muscle myosin II or alpha-catenin led to the formation of mazes, rather than long ridges (alae) on the midline; yet, these same knockdowns did not appreciably affect the pattern of circumferential bands (annuli). Imaging epidermal F-actin and cell-cell junctions revealed that longitudinal apical-lateral and apical-medial AFBs, in addition to cortical meshwork, assemble when the fused seam narrows rapidly; and that discontinuous junctions appear as the seam gradually widens. Ultrastructural analyses showed three protrusions beneath an interim matrix at peak of constriction, then relax to form a pocket in which the final ECM is deposited. Knocking-down actin abrogated the lateral pattern of two interim matrix (sheath) components. However, the circumferential pattern of the sheath remained. This and other findings contradict the model the annuli are patterned by circumferential actin filament bundles (CFBs). Instead, CFBs may comprise a temporary musculoskeletal system assembled to withstand the molt. Finally, knocking-down specific components of the sheath resulted in cuticle mazes. We propose that dynamic interactions among cortical actin networks, cell-cell junctions and apical matrices together control pulsatile constriction and pre-pattern the alae. Cell-aECM interactions may likewise affect outcome of AC in higher metazoans.

INTRODUCTION

Polarized epithelial cells give rise to various architecturally and functionally distinct structures that either include or adjoin specialized apical extracellular matrices (aECMs) in contact with the environment. Examples include the stereocilia on auditory hair cells and microvilli on kidney and intestinal epithelia, which comprise projections from live cells embedded in amorphous gels; human hair and fingernails, which comprise inviable cells covered by organized extracellular molecules; and tooth enamel, which is an acellular, mineralized matrix. Human mutations that affect related aECM components cause deafness, polycystic kidney disease and abnormal teeth (Devuyst et al., 2017; Legan et al., 2005; Masuya et al., 2005; Muller and Barr-Gillespie, 2015). Many of these matrices are shed and replaced to some extent; aberrant co-option of normal replacement processes in cancer is lethal (Cox and Erler, 2011; Lu et al., 2012). Despite the medical significance of the above-mentioned structures, the morphogenetic processes that sculpt such integumentary organs and appendages are not yet understood.

Development of many epithelial tissues and organs involves selective constriction of the apical surface of one or several epithelial cells. Resulting changes in cell shape are essential for morphogenetic processes ranging from gastrulation to the formation of buds and branches (Kim et al., 2013; Martin et al., 2010; Vasquez et al., 2014). The mechanical networks that drive apical constriction (AC) comprise three fundamental components: actomyosin filaments and/or bundles that generate contractile forces; cell-cell junctions that connect to actomyosin filaments and route forces among cells; and cortical flows, which promote assembly of cortical actin filaments at regions under tension (Martin and Goldstein, 2014). Fine spatial and temporal regulation of actomyosin contractility allows for precise and contextual shape changes. Although these mechanical networks are well characterized, the extent to which their fundamental components shape apical matrices is unclear. Moreover, the contributions of apical matrix components to the tissue-level outcomes of AC remain enigmatic. This gap relates to the current state of our basic knowledge regarding the biochemical composition, biophysical properties and physiologic functions of apical matrices.

The cellular and molecular components of mechanical networks that drive apical constriction are conserved between nematodes and mammals. The *C. elegans* cuticle is a multi-layered apical matrix produced by underlying cells and syncytia similar to simple epithelia of mammals (Page and Johnstone, 2007). The cuticle for the first larval stage is produced late in embryogenesis (Priess and Hirsh, 1986). Larval cuticles are shed and replaced with a progressively larger structures during each of the four molts characteristic of post-embryonic development (Knight et al., 2002; Sulston and Horvitz, 1977). Collagens are the major structural components of acellular worm cuticles (Cox et al., 1981a; Johnstone, 1994; Meli et al., 2010; Sapio et al., 2005), rather than the polysaccharide chitin comprising the exoskeletons of arthropods (Fabritius H., 2011). The apical-lateral junctions among epithelial cells and syncytia in *C. elegans* are analogous to those found in vertebrates and insects. Worm junctions contain two distinct molecular complexes (Pasti and Labouesse, 2014). The complex subjacent to the apical membrane comprises homologs of α-catenin (HMP-1), ß-catenin, p120-catenin, e-cadherin, and the Zonula Occludens (ZO) family (ZOO-1), which are canonical components of adherens junctions (AJs) (Costa et al., 1998; Loveless and Hardin, 2012). The second, more basal, molecular complex contains the worm homolog of *Drosophila* Discs-large (DLG-1) and a nematode-specific coiled-coil protein named AJM-1 (Koppen et al., 2001; McMahon et al., 2001). Additionally, *C. elegans* is a model organism amenable to genetic manipulation, live imaging, and quantitative analyses. This provides a tractable system to study the relationship between canonical AC networks and aECM patterning.

The illustrations in Figure 1 represent both prior knowledge of worm anatomy directly relevant to this report and our major findings regarding cell and molecular dynamics within the epidermis and renovation of apical matrices across the larval-to-adult transition. As depicted, the epidermis of *C. elegans* larvae consists mainly of the bilateral seam cells, which form rows along the long axis of the body, and hyp7 syncytium, which includes 139 nuclei in adults

(Sulston and Horvitz, 1977; Yochem et al., 1998) and covers most of the body. The stem cell-like seam cells undergo one round of asymmetric division early in each of the four larval stages. The posterior daughters remain in the seam while the anterior daughters fuse with hyp7. During the larval-to-adult transition, seam cells undergo homotypic fusion, becoming bilateral syncytia, and enter persistent cell-cycle quiescence (Sulston and Horvitz, 1977). Most of the seam is confined by the hyp7 syncytium, anchoring to hyp5 and the phasmid sensilla in the head and tail of the worm, respectively (White, 1988), overlying apical ECM and underlying basement membrane. Notably, the seam syncytium can be modeled as a pressurized cylinder sealed at both ends, wherein unbalanced axial and transverse forces produce hoop stress –similar to blood vessels and other tubular organs. The adjacent hyp7 syncytium has four discernable sub-regions: thick bilateral regions; dorsal and ventral ridges; and thin segments spanned by hemidesmosome plaques that anchor the underlying body wall muscles to the ECM (Bosher et al., 2003). In sum, the unique geometry of the epidermis in *C. elegans* presents noteworthy mechanical constraints.

Three longitudinal ridges called alae comprise the most obvious feature of the adult-stage cuticle (Fig. 1, young adult). Because the alae arise above the syncytial seam during the larval-to-adult transition, numerous studies vis-à-vis the succession of temporal cell fates have scored alae formation as a proxy for maturation of the epidermis (Ambros and Horvitz, 1984). Despite this steady interest, the coordinated rearrangements among cytoskeletal components with the epidermis and extracellular macromolecules that shape the alae have not been described, during any developmental transition. Prior studies that relied on phalloidin staining of fixed animals did not detect cortical F-actin in the seam of larvae or adults (Costa et al., 1997). The mechanism underlying their formation in adults is unknown. The seam also synthesizes morphologically distinct alae in L1 and dauer, an alternative L3 triggered by environmental duress (Hu, 2007). Evenly-spaced circumferential bands (annuli) flanked by narrow furrows are found on the surface of all 5 larval and adult stage-specific cuticles (Page and Johnstone, 2007). Parallel rows of circumferentially-oriented cortical actin filament bundles (hereafter "CFBs") present in the lateral region of hyp7 in embryos are widely thought to pattern the annuli of L1 (Costa et al., 1997; Priess and Hirsh, 1986), but this hypothesis has not previously been tested by experimentation. The mechanism by which the annular pattern is propagated in the subsequent molts is unclear. Nonetheless, spacing of the annuli is thought to be similar in larvae and young adults (Cox et al., 1981b). More recent studies of adult animals carrying mutations that affect body morphology have shown that the frequency of annuli along the long axis of the body scales with size (Essmann et al., 2017). Collectively, these observations suggest that additional or alternative biophysical processes play a role in propagation of the annular pattern.

The prevailing model for the process of molting in nematodes and other ecdysozoans comprises three sequential steps: 1) detachment of the epidermis from the preexisting cuticle (apolysis); 2) synthesis of a new and larger cuticle directly beneath the old cuticle; and 3) escape from the old cuticle (ecdysis) (Aguinaldo et al., 1997; Jenkin and Hinton, 1966; Locke and Huie, 1979; Page and Johnstone, 2007; Truman, 1992). Because this model does not invoke a provisional enclosure, it fails to explain how nematodes and other squishy animals remain intact, rather than implode. We recently discovered and communicated that *C. elegans* actually produce an interim apical ECM (sheath) at the start of every molt, which is shed together with the old cuticle at ecdysis (Katz, 2015). Notably, the sheath has a pattern similar to the emergent cuticle for the upcoming, rather than passing, life stage. This temporary covering prevents the rupture of epithelial tissues during the molt.

We identified the larval sheaths through our ongoing studies of the fibrillin-like apical matrix protein FBN-1 and the molting cycle (Frand et al., 2005). FBN-1 is characterized by a Zona Pellucida (ZP) domain at the C-terminus. In general, ZP domain proteins comprise networks and/or fibrils in specialized, often ephemeral, apical matrices (Jovine et al., 2002) that function to withstand mechanical stress from surrounding tissues (Plaza et al., 2010). ZP domain

proteins can also play instructive roles in the morphogenesis and maintenance of epithelial organs (Plaza et al., 2010). In addition, recent reports of other sheath components have also identified ZP domain proteins (Forman-Rubinsky et al., 2017).

Here, we describe a morphogenetic mechanism that integrates apical constriction with remodeling apical extracellular matrices. Therein, a pulse of anisotropic constriction generates transient epithelial protrusions coupled to an interim apical matrix, which then patterns long durable ridges on *C. elegans* cuticles. Moreover, we provide several lines of evidence that transient CFBs found in laterals regions of hyp7 are elaborations of previously unrecognized actin cables in quadrants of hyp7 overlying body wall muscles, rather than form factors for the annular bands found on the surface of all 5 stage-specific cuticles.

MATERIALS AND METHODS

Strains and Molecular Biology

C. elegans strains used in this study are listed in Table S1. Strains were maintained under standard conditions and cultivated at 25ºC unless otherwise specified (Brenner, 1974). For synchronization, gravid worms were bleached to isolate eggs, hatchlings arrested in starvation-induced L1 diapause, and released from diapause by plating on NGM seeded with *E. coli* OP50-1. Selected behaviors were scored to bin worms prior to mounting them on slides: locomotion and feeding indicated non-molting worms; quiescence indicated molting worm (Cassada and Russell, 1975); and idiosyncratic movements used to escape larval cuticles indicated ecdysis (Singh and Sulston, 1978). The precise stages of L4 and adult worms were further determined based on the shape of the gonad, vulva and lateral epidermis (Hubbard and Greenstein, 2005; Mok et al., 2015; Sulston and Horvitz, 1977). Cuticle caps over the mouth were indicative of worms undergoing molts (Monsalve et al., 2011). Strains with conditional alleles were propagated at permissive temperature (15ºC) and cultivated at restrictive temperature (25ºC) following release from starvation-induced L1 diapause. Bacterial-mediated RNA-interference (RNAi) was performed as described (Fraser et al., 2000; Kamath and Ahringer, 2003; Timmons et al., 2001), except that NGM (nematode growth medium) plates were supplemented with 8mM, rather than 1mM, isopropyl β-D-1-thiogalactopyranoside (IPTG). As a control, worms were fed the same *E. coli* HT115(DE3) transformed with pPD129.36. Upon induction by IPTG, such bacteria produce short dsRNA molecules that does not match any annotated gene of *C. elegans*.

Table S2 describes the oligonucleotides used in this study. Phusion High Fidelity Polymerase (NEB) was used to amplify DNA for sequencing and cloning. Taq Polymerase (NEB) was used for PCR-based genotyping. Gibson assembly (NEB) and standard cloning reactions were used to construct fusion genes and corresponding plasmids. To create the *elt-5p::rde-1::sl2-mcherry::unc-54* 3'-UTR fusion gene housed in pSK08, the promoter of *elt-5*, which corresponds to nucleotides 1910072-1913471 of chromosome IV (GenBank: NC_003282); the coding region of *rde-1*, which corresponds to nucleotides 9988043-9991614 of chromosome V (GenBank: NC_003283); coding sequence for *mCherry* (GenBank: KT175701), *sl2* (GenBank: LK928133); and the *unc-54* 3'-UTR cassette from pPD95.75 were combined. To construct the *dpy-7p::rde-1::sl2::nls-gfp::unc-54* 3'-UTR fusion gene housed in pSK38, the minimal promoter of *dpy-7*, which corresponds to nucleotides 7537789-7537869 and 7537914-7538219 of chromosome X (GenBank: NC_003284); the coding region of *rde-1*; *SL2*; and the *nls-gfp::unc-54* 3'-UTR cassette from pPD95.73 were united. To construct the *dpy-7p::utrnch::dsred::unc-54* 3'-UTR fusion gene housed in pSK26, the promoter of *dpy-7* (as above); the coding sequence for the first CH domain (residues 1-261) of human Utrophin (GenBank: LX69086); the coding sequence for *dsRed* (GenBank: HQ418395); the *unc-54* 3'-UTR cassette from pPD95.81; and the pUC57 backbone were combined. To construct the *elt-5p::utrnch::gfp::unc-54* 3'-UTR fusion gene housed in pSK34, the promoter of *elt-5*; the sequence encoding UTRNCH; and the *gfp::unc-54* 3'-UTR cassette and backbone from pPD95.81 were united. All variants of plasmids pPD95 were gifts from Andy Fire.

Towards the production of a full-length *fbn-1::mCherry* fusion gene, genomic DNA spanning 3.6kb of upstream sequence and exons 1-14 of *fbn-1k* (Genbank: JQ990128); cDNA spanning exons 14-22 isolated from pMH281 (Maxwell Heiman, Harvard Medical School); and genomic DNA spanning exons 21-25 and the 3'-UTR of *fbn-1k* were combined in plasmid pSK27. The latter fragment was modified by insertion of an in-frame *NotI-mCherry-NotI* cassette between the codons for H2418 and V2419 of *fbn-1k*. *mCherry* was isolated from KP1272 (Joshua Kaplan, HMS). A 7.4 kb region of genomic DNA spanning the entire promoter and exons 1-2 of *fbn-1* was amplified separately. pSK27 and the purified PCR product were co-injected at an equimolar ratio, allowing for homologous recombination *in vivo* (see below). The genomic DNA present in the full length (fl) *fbn-1::mCherry* fusion gene corresponds to nucleotides 7619229-7641053 of chromosome III (GenBank: LK928224). To construct the *noah-1::sfGFP::noah-1* translational fusion gene housed in pCM05, regulatory and coding regions of *noah-1* were amplified from genomic DNA (nucleotides 5874389-5883950 of chromosome I, GenBank: LK927608) and cloned into a NotI-filled derivate of pCR-Blunt II-TOPO (Invitrogen). A *NotI-sfgfp-NotI* cassette was inserted in-frame between the codons for P624 and V625 of *noah-1a* (Genbank: NM_170870). The corresponding NotI site was created using a Q5 mutagenesis kit (Invitrogen). Superfolder (sf) GFP was isolated from pCW11 (Max Heiman, Harvard University).

All extrachromosomal arrays were generated by microinjection of young adults with mixtures containing a total of 100ng/µl DNA. To generate *aaaEx37*, pSK08 (5ng/µl); *ttx-3::gfp* (40ng/µl); and pRS316 (55ng/µl) were co-injected into JK537 *rde-1(ne219)*. To generate *aaaEx162*, pSK38 (5ng/µl); *ttx-3::dsred* (40ng/µl); and pRS316 were co-injected into JK537. To generate *aaaEx108*, pSK26 (0.5ng/µl); *ttx-3::gfp*; and pRS316 were co-injected into N2. To generate *aaaEx117*, pSK34 (5ng/µl); *ttx-3::gfp*; and pRS316 were co-injected into N2. Optimal plasmid concentrations used to generate tandem *utrnch* arrays were empirically determined by titration. UTRNCH signals were readily detected in the resulting transgenic animals, while phenotypes associated with high levels of UTRN were not observed. To generate *aaaEx78[fl-fbn-1::mCherry::fbn-1],* pSK27 (2.5 ng/µl); the above-mentioned PCR product (1.15 ng/µl); *ttx-3p::gfp*; and pRS316 were co-injected into N2. To generate *aaaEx167*, pCM05 (1ng/µl); *ttx-3::dsred*; and pRS316 were co-injected into ARF379. Resulting transgenic lines were out-crossed to N2 to remove *aaaIs12*. Extrachromosomal arrays were integrated into the genome by UV irradiation at 450 kJ using an FB-UVXL-1000 (Fisher Scientific). Strains with newly-integrated arrays were back-crossed to JK537 or N2 4 to 6 times prior to further analyses.

To knockdown *actin* by bacterial-mediated RNAi, we used the clone for *act-2* present in the Ahringer library (Kamath and Ahringer, 2003). Towards knocking-down *nmy-1* (Genbank: LK927643), 1121bp of genomic DNA from exon 10 was cloned into pPD129.36, the standard expression vector for dsRNAs. For *zoo-1* (GenBank: NM_001026515), cDNA spanning exons 1-7 was cloned into pPD129.36, as previously described (Lockwood et al., 2008). For *noah-1* (GenBank: LK927608), 1024bp from exon 6 was cloned into pPD129.36. Each of the resulting plasmids (pSK43, pSK44 and pCM15) was verified by Sanger sequencing and used to transform *E. coli* strain HT115(DE3).

DiI Staining of Cuticles

DiI staining to visualize cuticle structures was performed basically as described (Schultz and Gumienny, 2012), except that glass pipettes were used to transfer samples in lieu of Triton X-100. Briefly, approximately 600 adult worms were incubated in 400µl of 30 µg/mL DiI (Sigma) in M9 for 3 hours, shaking at 350rpm. Worms were then washed 1X in M9 buffer, re-suspended in 100µl of M9, and dispensed to a 6cm NGM plate seeded with *E. coli* OP50-1. To remove excess unbound dye, worms were allowed to crawl on the plate for 30min prior to imaging.

Microscopy and Image Analyses

Worms were anesthetized with sodium azide (2.5%) in M9 buffer and mounted on 2% agarose pads. A Zeiss Axioplan microscope with an attached Hamamatsu Orca ER CCD camera was

used for compound microscopy. Images were acquired and analyzed using the software package Volocity 6.3 (PerkinElmer). A Zeiss LSM 5 PASCAL microscope controlled by ZEN 9.0 software was typically used for confocal microscopy. A Zeiss LSM880 laser scanning confocal microscope was used as specified. Measurements were made using Volocity 6.3 (PerkinElmer), ImageJ (Version 1.48v, NIH), and Fiji (Schindelin et al., 2012). Volocity was used to measure fluorescence intensity in manually-selected, similarly-sized regions along the margins of hyp7. Four ROIs were assayed per worm. The ImageJ plugin FibrilTool was used to measure anisotropy (Boudaoud et al., 2014). For each worm assayed, 6 values were obtained by subdividing the lateral region of hyp7 into 3 dorsal and 3 ventral ROIs, each approximately 400μm^2.

For transmission electron microscopy (TEM), synchronized wild-type (N2) animals were collected, washed once in 8% ethanol and M9, and washed 3 times in PBS over a period of 30 mins. Specimens were suspended in 2.5% glutaraldehyde, 1% paraformaldehyde and 0.1M sucrose in PBS; incubated for 2 hours on ice; and incubated for 16 hours at 4°C. Samples were washed, post-fixed in 1% OsO4, and dehydrated by serial immersion in graded ethanol solutions. Samples were then passed through propylene oxide, embedded in serial steps using mixtures of propylene oxide and Epon 812, and cured at 60°C for 48 hrs. An RMC MTX ultramicrotome was used to cut 60 nm-thick sections, which were stained with uranyl acetate and lead citrate. Sections were observed using a 100CX JEOL electron microscope.

Statistical Analyses and Image Presentation

GraphPad Prism 6 and Microsoft Excel 15.21 were used for statistical analyses. All micrographs were prepared for publication using Adobe Photoshop v13.0 and Adobe Illustrator v16.0.

RESULTS

Actin and NMII pattern longitudinal, rather than annular, folds in adult cuticles.

To evaluate the role of actin filaments and/or bundles in patterning emergent cuticles, we used both bacterial-mediated RNA-interference (RNAi) and conditional mutations to knockdown actin and non-muscle myosin II (NMII) in while larvae developed and then examined the lateral surface of young adults. Longitudinal ridges overlying seam syncytia (alae) were directly observed by DIC microscopy. Raised circumferential bands overlying hyp7 (annuli) were detected by staining animals with the fluorescent lipophilic dye DiI prior to observation (Schultz and Gumienny, 2012).

Five genes of *C. elegans* encode actin. Epidermal cells and syncytia express *act-1, -2*, *-3* and possibly *-4* but evidently not *act-5* (MacQueen et al., 2005; Sarov et al., 2012; Willis et al., 2006). To simultaneously knockdown *act-1*, *-2*, *-3* and *-4*, we selected a dsRNA trigger complementary to all four transcripts. Further, we customized and applied an established experimental paradigm to selectively knockdown *actin* in the seam or hyp7. This system entails the tissue-specific expression of wild-type *rde-1*, which encodes the worm homolog of Argonaute, in *rde-1(null)* mutants otherwise insensitive to siRNAs (Qadota et al., 2007; Steiner et al., 2009). Epidermis-specific knockdown of *actin* minimized the larval lethality associated with systemic RNAi of *actin* over the 42-hour course of larval development. Exposure to *actin* dsRNAs for only 30 hours starting in the L2 stage also bypassed this lethality, allowing otherwise wild-type, *actin(RNAi)* larvae to develop into relatively small adults.

Preferential knockdown of *actin* in either the seam or hyp7 led to the formation of grossly misshapen patches of cuticle, which interrupted the three ridges characteristic of adult-stage alae (Fig. 2A). Patches with many tortuous, short ridges and discontinuous longitudinal ridges were observed on 93% of seam-specific *actin(RNAi)* animals and 89% of hyp7-specific *actin(RNAi)* animals (n≥100). Hereafter, we refer to such patches as “mazes.” The most extensive mazes lacked detectable dorsal and ventral ridges. Such deformities were not found on the lateral surface of *rde-1(null)* mutants fed the same bacteria transformed with empty vector. However, mazes were observed on 89% of wild-type animals following acute exposure

to *actin* dsRNAs (Fig. 2A-B). Some mazes appeared next to large (>5μm) stretches of cuticle devoid of longitudinal ridges. These stretches uniformly aligned with gaps in the subjacent seam syncytium detected by DIC and fluorescence microscopy. These gaps may be attributable to the loss of seam nuclei during aberrant, larval-stage cell divisions. Accordingly, our scoring rubric prioritized mazes over large gaps and minor deformities found along the midline of any particular worm.

Two genes of *C. elegans* encode NMII heavy chains approximately 47% identical to human NMMHC-IIB (Piekny et al., 2003). We used *nmy-1(RNAi)* and conditional *nmy-2(ts)* alleles to partially inactivate NMII throughout this study. Mazes, by and large extensive, were observed on 94% of *nmy-1(RNAi); nmy-2(ne3409ts)* double mutants and 97% of *nmy-1(RNAi); nmy-2(ne1490ts)* double mutants raised at restrictive temperature (Fig. 2A-B). Minor deformities in the alae such as small divots were observed on 82% of *nmy-1(RNAi)* single knockdowns and a minority of *nmy-2(ne3409ts)* and *nmy-2(ne1490ts)* single mutants. Collectively, these findings suggest that actomyosin networks within the seam and hyp7 syncytia cooperatively shape the adult-stage alae. The *nmy-1* and -2 genes may act redundantly or cooperatively in this context.

As described, DiI labels raised segments of the cuticle including alae and annuli but does not impregnate adjacent furrows (Schultz and Gumienny, 2012). As expected, DiI stained scores of evenly-spaced circumferential annuli on dorsolateral and ventrolateral surfaces of wild-type adults (Fig. 2C). DiI also labeled evenly-spaced, annular bands on the surface of *actin(RNAi)* adults, while labeling mazes on the lateral midline. The frequency of annular bands appeared greater on *actin(RNAi)* animals than age-matched controls, consistent with the small size of *actin(RNAi)* adults and the reported scaling of these two morphometric features (Essmann et al., 2017). DiI likewise stained evenly-spaced, annular bands on the surfaces of *nmy-1(RNAi)* single knockdowns, *nmy-2(ts)* single mutants and *nmy-1(RNAi) nmy-2(ts)* double mutants, which had grossly misshapen alae (Fig. 2C). Because DiI consistently saturated the alae, signal in adjacent regions of the cuticle often appeared less intense and more variable among isogenic worms. The formal possibility that these knockdowns lead to subtle defects in the curvature or texture of annuli cannot be eliminated using this approach. Nonetheless, we found no evidence that regenerating the pattern of annuli in adult cuticles requires actin or NMII, whereas *de novo* patterning of the alae clearly required the corresponding genes. This particular finding contradicts the widely-accepted model that transient CFBs present in hyp7 during molts pattern the annuli of nascent cuticles (Costa et al., 1997).

AJ components that interact with actin networks shape the adult-stage alae.
To evaluate the role of cell-cell junctions in patterning emergent cuticles, we similarly used RNAi and a hypomorphic allele to knockdown key AJ components while larvae developed and then examined the lateral surface of young adults. As described, HMP-1/α-catenin is the actin-binding component of cadherin-catenin complexes (CCCs) that mechanically link the various epidermal cells of *C. elegans* (Costa et al., 1998; Kang et al., 2017; Loveless and Hardin, 2012). ZOO-1 cooperatively recruits actin bundles to AJs (Lockwood et al., 2008). We used the substitution mutation *hmp-1(fe4)* because the corresponding protein has decreased affinity for actin but approximately half of the homozygous mutants complete embryonic and larval development (Maiden et al., 2013; Pettitt et al., 2003). We used RNAi of *zoo-1* to sensitize the genetic background. Mazes were observed on the surface of 46% (n=107) of *zoo-1(RNAi); hmp-1(fe4)* double mutants (Fig. 3A-B). Continuous dorsal and ventral ridges framed the majority of these mazes, as observed upon attenuated RNAi of *actin* in wild-type adults (Fig. 2A). Further reduction of *hmp-1* activity may well result in extensive mazes. DiI labeled periodic, annular bands on the dorsolateral and ventrolateral surfaces of all (n=17) *zoo-1(RNAi; hmp-1(fe4)* double mutants, despite the high penetrance of misshapen alae (Fig. 3C). The DiI signal and background fluorescence appeared more intense on *hmp-1(fe4)* mutants than wild type adults. This difference may result from relatively inefficient removal of unbound dye through free movement on NGM plates, as the locomotion of *hmp-1(fe4)* adults was visibly impaired. Thus, genetic manipulations that compromise the ability of AJs to transmit forces between

actomyosin networks in the seam and hyp7 disrupted the pattern of adult-stage alae but had little, if any, effect on propagation of the pattern of annuli from L1- to adult-stage cuticles.

Cortical actin dynamics linked to pulsatile apical constriction of seam syncytia

To further investigate the role of actin networks and AJs in shaping emergent alae, we tracked the distribution of F-actin at the cortex of seam cells and syncytia in animals developing from the L3 to the adult stage (Fig. S1, Fig. 4). For this purpose, we constructed a genetically-encoded sensor for F-actin comprising the Calponin homology domain (CH) of human Utrophin (UTRN) tagged with GFP and driven by the seam-specific promoter of *elt-5* (Koh and Rothman, 2001). This approach enabled highly-sensitive live-imaging because UTRNCH::GFP binds F-actin selectively and reversibly; in addition, UTRNCH::GFP has no appreciable effect on actin rearrangements when expressed at practical levels (Burkel et al., 2007; Moores and Kendrick-Jones, 2000). To capture both cell and molecular dynamics germane to morphogenesis of the alae, we combined AJM-1::mCHERRY, an established marker for adherens junctions (Koppen et al., 2001), with the seam>UTRNCH::GFP sensor. To achieve fine temporal resolution, we isolated precisely staged transgenic nematodes as follows: We selected ~60 individuals transiting the L3/L4 molt from synchronously developing populations and watched them; the time when a given worm emerged in L4 was set to zero; we then collected cohorts of ~7 worms at regular ~1hr intervals and imaged both GFP and mCherry near the apical surface of the later epidermis using confocal fluorescence microscopy.

As described, each row of seam cells undergoes homotypic fusion sometime during the L4 stage, forming bilateral syncytia (Fig. 4A). Homotypic fusion follows the last round of asymmetric division and precedes the onset of the final (L4/A) molt (Podbilewicz and White, 1994). The seam syncytia go on to make the adult-stage alae during the molt. As shown in Fig. S1, the rectangular seam cells of late L3 larvae were connected to each other and hyp7 by AJs incorporating AJM-1::mCherry. UTRNCH::GFP labeled F-actin within cortical meshworks and alongside AJs. The seam cells became more ellipsoidal during the L3/L4 molt and divided shortly thereafter. The anterior daughters were excluded from the seam as the posterior daughters reconnected (Fig. S1). Surprisingly, we found seam syncytia, rather than individual cells, in all nematodes imaged 3-hours after emergence in L4 (Fig. 4B). Thus, homotypic fusion occurred much earlier than expected based on common description and illustrations of the seam cell lineage (Herman, 2006). Capturing the dynamic redistribution of cortical actin during asymmetric division, cytokinesis, migration of the posterior daughters and homotypic fusion of the seam cells validated our key reagents and approach.

Straightaway, the apical surface of seam syncytia narrowed, as AJs demarcating the dorsal and ventral margins drew closer together (Fig. 4B, 3hrs). The apical surface of the seam then widened slowly, as the AJs spread apart over the following 4-5hrs. This interval included much of the L4/adult molt (Fig. 4B, molt). The observed shape changes hinted at a pulse of anisotropic constriction on the D-V (transverse) axis followed by gradual relaxation. As described below, concurrent changes in the ultrastructure of the epidermis detected by transmission electron microscopy (TEM) further substantiated this model (see Fig. 6).

Two longitudinal actin bundles rapidly assembled at the cortex of seam syncytia, co-localizing with AJs along the dorsal and ventral margins (Fig. 4B, arrows). These particular actin bundles persisted as the seam narrowed. The extent to which longitudinal actin bundles overlapped with AJs diminished as the seam widened. Instead, we detected spikes of F-actin orthogonal to the margins (Fig. 4B, chevrons). These spikes increased in size but decreased in number as larvae entered the molt and emerged as young adults. This dramatic reorientation of marginal F-actin relative to AJs suggested a corresponding change in the routing of forces between the seam and hyp7.

Two more actin bundles assembled in the middle of seam syncytia (Fig. 4B, dashes). These medial-axial bundles moved closer together as the seam narrowed, spread apart as the seam

widened, and endured the process of molting. Cortical meshworks were detected at all times but relatively difficult to discern in narrow syncytia. At the apex of apical constriction, the pattern of longitudinal actin cables near the surface of seam syncytia bore a striking resemblance to the adult-stage alae, manifest ~6hrs later.

To identify cortical actin structures that most likely generate or route mechanical forces relevant to patterning the alae, we considered that tension *per se* stabilizes actomyosin filaments and related adhesive complexes (Hannezo et al., 2015; Wu and Yap, 2013). For this reason, we examined the distribution of AJs and cortical actin in NMII knockdowns transiting the L4/A molt (Fig. 4C). AJs demarcating the dorsal and ventral margins of seam syncytia were tortuous but typically farther apart in *nmy-1(RNAi); nmy-2(ne3409ts)* double mutants than age-matched transgenic nematodes. Distension of the seam syncytia seemed to account for the girth of cuticular mazes found on *nmy-1(RNAi); nmy-2(ts)* adults (Fig. 2A). Further, medial-axial actin bundles and cohesive cortical meshworks were not detected in the seam syncytia of *nmy-1(RNAi); nmy-2(ne3409ts)* double mutants, but were found in control specimens (Fig. 4C, dashes). Distended seam syncytia lacking medial-axial actin bundles and cohesive cortical meshworks were likewise observed in *nmy-1(RNAi); nmy-2(ne1409ts)* double mutants. Qualitatively similar but less severe abnormalities were observed in the corresponding single mutants (Fig. 4C). In contrast, spikes of F-actin orthogonal to AJs were readily detected in *nmy-1 nmy-2* double and single knockdowns, as well as control specimens. Thus, the assembly and/or persistence of medial actin cables and meshworks near the apical surface of seam syncytia depends on NMII more than the assembly and/or persistence of peripheral spikes. Taken together, these findings suggest that cortical tension contributes to apical constriction of the seam syncytia, its measured relaxation and/or maintenance of the resulting shape of seam syncytia, which are distinct but likely interdependent processes.

Tension affects dynamics of F-actin at margins, rather than CFBs in lateral hyp7.
As our initial findings indicated that actomyosin networks in both the seam and hyp7 syncytia contribute to morphogenesis of the alae, we went on to track the distribution of cortical actin in hyp7 across the larval-to-adult transition (Fig. 5, Fig. S2). For this purpose, we constructed a similar but distinct F-actin sensor comprising UTRNCH tagged with dsRED and driven by the hypodermal-specific minimal promoter of the cuticle collage gene *dpy-7* (Johnstone et al., 1992). Longitudinal actin bundles were detected along the lateral margins of hyp7 throughout L4 and the L4/A molt (Fig. 5A & B). The intensity of corresponding signals peaked ~6hrs after larvae emerged in the L4 stage and plummeted as adults escaped from the larval cuticle. Spikes of F-actin orthogonal to the lateral margins were also detected in molting animals. To evaluate the possibility that actin at the margins of hyp7 regulates changes in seam cell shape, we examined these structures after genetic inactivation of NMII. Signals from hyp7>UTRNCH::dsRED were barely detectable at the boundary between hyp7 and seam syncytia in *nmy-1(RNAi); nmy-2(ne3409)* double mutants molting from L4 to the adult stage (Fig. 5D). The average fluorescence intensity at this boundary was 72±22 a.u. (N=5) in double mutants, compared to 116±20 a.u. (N=7) in transgenic but otherwise wild type animals (Fig. 5E). Finding that actomyosin contractility maintains actin bundles on the hyp7 side of AJs suggests that these force-transmitting complexes regulate the gradual widening of the seam syncytia during the molt.

Cortical meshworks were detected in the lateral (thick) regions of hyp7 syncytia ~3hrs after larvae emerged in the L4 stage. Parallel arrays of circumferentially-oriented actin filament bundles (CFBs) assembled near the apical surface of hyp7 over the following 3hrs; persisted through the molt; and then abruptly collapsed. These dynamics were substantiated by anisotropy values (a metric for parallel alignment) of UTRNCH::dsRed signals in this region of interest. On average, anisotropy values increased 5-fold during the L4 stage, remained high for most of the L4/A molt, plummeted at ecdysis, and returned to base-line in young adults (Fig. 5C). We further examined the status of CFBs in hyp7 upon inactivation of NMII. CFBs persisted in virtually all *nmy-1(RNAi); nmy-2(ne3409)* double mutants and corresponding single mutants

molting from L4 to adult (Fig. 5D). In one double mutant, neither the seam syncytium nor CFBs were detected, indicating an atypically severe phenotype. Consistent with these observations, no significant differences were found among mean anisotropy values for UTRNCH::dsRED in mutants versus control (Fig. 5F). However, individual anisotropy measurements were twice as variable in double mutants. Assembly, maintenance and organization of the CFBs appeared largely independent of contractility, and thus unlikely to regulate seam shape. Moreover, since increased variability in anisotropy associated with NMII knockdown was not mirrored by irregular patterning of annuli (Fig. 2C), CFBs seem unlikely to pattern the annuli. Rather, the observed timing of CFB assembly and disassembly suggested an alternative function.

Transient CFBs in lateral hyp7 connect to stable CFBs in hyp7 over muscle.
During the above-mentioned study, we noticed that some of the transient CFBs detected in the lateral region of hyp7 across the L4-to-adult transition extended into the quadrant of hyp7 overlying body wall muscle (Fig. 5D and Fig. S2). These previously unrecognized CFBs in hyp7 overlying body wall muscle (mCFBs) were consistently observed L4 larvae, molting animals, and adults (Fig. S2A and B). The mCFBs were situated between *Ce.* hemidesmosomes (*Ce*HDs) (Fig. S2B and C), labeled by MUP-4::GFP, which is an apical ECM receptor of *Ce*HDs (Hong et al., 2001), as well as VAB-10A::GFP, which is the core *Ce*HD spectraplakin (Morrissey et al., 2014). These findings suggest that mCFBs are a component of stable, cell-ECM attachment complexes distinct from *Ce*HDs.

Ultrastructure of the epidermis during deposition of the alae.
Our findings show that the contractile actomyosin cytoskeleton coupled to tension-bearing cell-cell junctions was required to shape the three dimensional cuticle alae. Does the tissue ultrastructure undergo concomitant changes during this process? Figure 6A shows TEM micrographs captured by Singh and Sulston in 1978 in a pioneering early study of the molt in *C. elegans* (Singh and Sulston, 1978). Apical constriction of the seam cortex was readily apparent in mid L4. The width of the seam, as determined by the distance measured between the apical junctions with hyp7, decreased by approximately 3.5-fold. This was accompanied by upward blebbing of the apical membrane, taking the shape of three protrusions underneath the L4 cuticle. Two mounds were situated above the seam-hyp7 junctions, and the third in the middle of the seam cortex.

Inward deformation of the apical membrane of the seam and hyp7 syncytium followed in the L4-to-adult molt, forming a large pocket in which the adult alae are deposited (Fig. 6B). The distance between the dorsal and ventral apical junctions of the seam increased, reflecting the gradual relaxation of apical constriction detailed above. The progressive deposition of the adult alae underneath the L4 cuticle was evidenced by the increasing size of the ECM ridges (Fig. 6B i-iii). As the seam widened, the position of the seam-hyp7 junctions shifted relative to the growing alae ridges, whose periodicity did not change appreciably during the molt. Secretory granules were also visible within the seam syncytium. These vesicular structures appeared to be evenly distributed near the apical membrane of the seam instead of localizing to either furrows or ridges. This would suggest that there are no specific sites of secretion. Notably, as the alae grew, the L4 cuticle seemed to gradually thin. In adults, we detected the characteristic three ridges of the adult alae, and the surface of seam and hyp7 syncytia followed the contour of the body (Fig. 6C).

Lastly, we also identified extracellular material between the L4 cuticle and underlying tissue that did not resemble mature cuticle, either of the L4 or the adult. This ECM was most prominent in the micrograph of a mid-L4 animal (Fig. 6A), where a continuous structure covered all three membrane protrusions. Remnants of this structure were detected in the early phases of the molt (Fig. 6Bi and ii). We identified this material as sheath, the temporary matrix deposited before the permanent ECM and subsequently shed with the old cuticle at the end of the molt. (Katz, 2015).

Provisional sheaths relay cortical actin dynamics to fixed patterns in apical matrices. Based on the spatial and temporal correlations among the longitudinal actin bundles present in seam syncytia at the apex of constriction (Fig. 4B); transient protrusions from the apical surface of seam syncytia (Fig. 6A); and the appearance of longitudinal bands in the provisional sheaths of animals molting from L4 to the adult stage (Fig. 7), we hypothesized that cortical actin dynamics were mechanically coupled to this short-lived aECM. As an initial test of this hypothesis, we determined the effect of attenuated *actin* RNAi on the pattern of two components of the L4/A sheath; namely, the ZP-domain proteins FBN-1 and NOAH-1. Both *fbn-1* and *noah-1* emerged from a preliminary, RNAi-based screen for knockdowns unable to molt (Frand et al., 2005). Thereafter, we constructed full-length (FL) *fbn-1::mCherry* and *noah-1*::*sfgfp* translational fusion genes within distinct extrachromosomal arrays (*aaaEx78* and *aaaEx167*). These arrays rescued the lethality caused by respective null alleles of *fbn-1* or *noah-1*, confirming the production of functional fusion proteins. As previously described and shown in Fig. 7A, circumferential bands of FL-FBN-1::mCherry corseted the body while larvae underwent molts and while embryos elongated. Longitudinal bands of FL-FBN-1::mCherry were also detected above the seam syncytia during the L4/A molt. The pattern of these bands presaged the forthcoming alae (Katz, 2015). Longitudinal and circumferential bands of NOAH-1::sfGFP were also detected above the seam syncytia during the L4/Adult molt (Fig. 7B). In this case, the fluorescent signal localized to four distinct stripes aligned with light-refractive regions of the nascent cuticle visible by DIC; these stripes likely correspond to temporary furrows flanking the emergent alae.

Following attenuated RNAi of *actin*, FL-FBN-1::mCherry localized to labyrinthine deformities, rather than longitudinal bands, overlying the lateral surfaces of emergent adult-stage cuticles (Fig. 7A). The abnormal pattern of FL-FBN-1::mCherry within the sheath matched the abnormal pattern at the surface of emergent cuticles detected by DIC. Attenuated RNAi of *actin* also led to the deposition of NOAH-1::sfGFP mazes perfectly aligned with misshapen furrows in the emergent cuticle above the seam syncytia (Fig. 7B). In contrast, the annular patterns of FL-FBN-1::mCherry and NOAH-1::sfGFP were superficially normal in *actin(RNAi)* animals, consistent with our initial findings that both epidermis-specific and systemic but attenuated RNAi of *actin* impaired *de novo* patterning of the alae, rather than propagation of the pattern of annuli.

The above-mentioned hypothesis further predicts that knocking-down certain sheath components will lead to deformities in apical ECMs. We therefore examined the lateral surfaces of young adults following attenuated but systemic RNAi of *noah-1.* Mazes and minor deformities in the alae were detected in 81% (N=100) of *noah-1(RNAi)* adults, but were not detected in same-day controls, consistent with our working model that provisional sheaths propagate cortical actin dynamics underlying transient changes in epithelial cell shape to sculpt more durable apical matrices.

Having conceived this working model and validated its key predictions in the context of the larval-to-adult transition, we asked whether a similar, if not identical, morphogenetic mechanism gives rise to the architecturally distinct alae of dauers. To address this question, we combined the conditional *daf-2(e1370)* allele, which confers a dauer-constitutive (Daf-c) phenotype at restrictive temperature, with our seam>UTRNCH::GFP sensor for F-actin and our FL-FBN-1::mCHERRY marker for the provisional sheaths of molting worms. We then imaged UTRNCH::GFP in live nematodes molting from L2d to dauer, a process that involves extreme radial constriction of the body. Early in the molting process, dense cortical meshworks including both longitudinal and transverse actin filaments and/or bundles were detected in rather wide seam cells (Fig. S3A). Later in the process, we detected spikes of actin orthogonal to junctions between seam cells and hyp7 in the very thin seam cells of fully constricted animals. We also imaged FL-FBN-1::mCHERRY across the L2d to dauer molt. The pattern of FL-FBN-1::mCHERRY in the corresponding sheath included five longitudinal stripes within a wide lateral band (Fig. S3B). While this pattern was markedly different from the sheaths of animals molting from L4 to the adult stage, the pattern of FBN-1 stripes yet again presaged the

shape of the forthcoming dauer-specific alae, which have four ridges that span most of the lateral surface of the cuticle (Fig. S3C). These observations are entirely consistent with temporal reiteration of a common morphogenetic mechanism.

DISCUSSION

Figure 8 provides a cohesive model for maturation of the epidermis and morphogenesis of the adult-stage alae in *C. elegans*. The progressive changes in tissue architecture and underlying rearrangements in the actin cytoskeleton depicted are based on the key results in this report and current knowledge regarding various dynamic mechanisms by which apical constriction shapes developing organs (Martin and Goldstein, 2014). Contrary to canonical examples of apical constriction, in which the area of the cell surface decreases in an isotropic manner, we have observed and described an anisotropic change. Here, the seam syncytium undergoes a rapid narrowing on the dorsal-ventral axis, followed by a gradual widening (Fig. 8A). This change in shape is clearly attributable to the forces generated by actomyosin filaments and propagated through adherens junctions, given that knocking-down either non-muscle myosin or actin-binding components of cell-cell junctions abrogates the otherwise uniform narrowing of the seam. Consistent with this model, the abundance of junctional F-actin in both the seam and hyp7 increase during constriction.

At the apex of constriction, three protrusions form in the apical membrane –one each above the dorsal and ventral seam/hyp7 junctions, respectively, and a third in the middle of the seam (Fig. 8B). These cellular blebs correspond to the localization of axial F-actin bundles in the seam at its narrowest. Concomitantly, an interim matrix or sheath is deposited between the effete L4 cuticle and the epidermis, templating the three ridges of the adult alae. Actin is required for sheath patterning; integrity of the sheath is in turn required for patterning the mature alae. Apical seam constriction is then followed by controlled relaxation and related widening of the syncytium. In the seam, the longitudinal F-actin bundles at the junctions are replaced by orthogonal actin spikes, although the medial-axial bundles persist through the L4/Adult molt. Similar specialized F-actin structures in the seam are not detected in immature seam cells or during prior larval-to-larval molts. Further, the entire contractile apparatus at the cortex of the lateral epidermis is disassembled at the end of the molt, as the animal sheds its larval cuticle and the sheath. Only the actin structures in regions of hyp7 overlying body wall muscle persist throughout.

These findings uncover a novel but likely conserved morphogenetic mechanism that links mechanical networks driving apical constriction with matrix dynamics. Given that the key intracellular and extracellular molecules are conserved between nematode and mammals, this new system is likely relevant to mammalian physiology and pathology.

ACKNOWLEDGEMENTS

Some strains used in this study were provided by the *Caenorhabditis* Genetics Center, which is funded by the NIH Office of Research Infrastructure Programs (P40 OD010440). We are grateful to Margot Quinlan, Alvaro Sagasti, and Larry Zipursky for helpful scientific discussions and critiques of this manuscript, and to Hannah Maul-Newby, Chloe Maybrun, and Dominic Williams for valuable technical assistance. We thank Margot Quinlan, John Kim, Eric Miska, and David Sherwood for strains and reagents. A Ruth L. Kirschstein National Research Service Award (GM007185 to SK), UCLA Dissertation Year Fellowship (SK), and a National Science Foundation Award (IOS 1258218 to ARF) supported this research.

FIGURE LEGENDS

Figure 1. Revised model for progression of the final molt and formation of the adult alae. Anatomical illustrations of the mid-section of *C. elegans* show changes in the epidermis, the actin cytoskeleton, and overlying matrices across the larval-to-adult transition. These drawings encapsulate relevant prior knowledge in the field and major findings described in this report.

Figure 2. Knockdown of epidermal actin and NMII leads to deformed alae but seemingly normal annuli. A) Representative DIC micrographs show the lateral surface of young adults of the indicated genotypes. Brackets demarcate the region overlying the seam syncytium. (Upper left) Yellow dashes mark the 3 longitudinal ridges, which are less refractive; black dashes mark adjacent furrows, which are more refractive. Arrows point to mazes, as defined in the text. The asterisk labels a large gap in the alae. Arrowheads point to minor deformities such as divots and breaks in otherwise continuous structures. **B)** Graph shows the frequency of above-mentioned deformities. As described, mazes were given top priority *post-hoc*, as each specimen was binned in one category. Values represent the weighted average of 2 independent trials. $P<0.001$ for all pairwise comparisons between control and *actin(RNAi)* or *nmy-1(RNAi)* cohorts of the strain by Fisher's exact test with Bonferroni's correction for multiple comparisons. **C)** Confocal fluorescence micrographs show Dil-stained cuticles of young adults. Arrows point to a wild-type annulus and similar structures in other images. Arrowheads point to malformed alae. (Upper right) Schematic shows the normal pattern of Dil-stained structures detected on adult cuticles. **A & C)** Scale bars = 5µm. Strains ARF330, ARF408, N2, WM179 and WM180 were imaged.

Figure 3. Knockdown of α-catenin and ZO-1 results in mazes on the lateral cuticle. A) DIC micrographs show the lateral surface of young adults. Brackets demarcate the region overlying the seam syncytium. In wild type, yellow and black dots mark the furrows and ridges of the alae along the A-P axis of the body, respectively (as in Fig. 2A). An arrow points to an instance of mazes, and an arrowhead points to a deformity classified as "other", which includes small discontinuities and divots. **B)** Graph shows the frequency of alae phenotypes in young adults of indicated genotypes. Each animal observed was binned in a single category, with mazes given priority over other alae defects. Values represent the weighted average of two independent trials. Outcomes were classified as superficially normal vs. abnormal alae to perform Fisher's exact test with Bonferroni correction for multiple comparisons, $^{n.s.}P>0.99$, $^{****}P<0.0002$. **C)** Confocal fluorescence micrographs show Dil-stained substructures in the cuticles of young adults. Arrows point to superficially similar circumferential bands (annuli); arrowheads point to instances of malformed alae. **A-C)** Imaged strains correspond to N2 and PE97. Scale bar = 5µm.

Figure 4. Dynamics of junctional and axial F-actin cables during pulsatile apical constriction of the seam. A) Diagrams show the position of the epidermal seam cells and syncytia in juvenile and mature *C. elegans*, respectively. The micrographs in panels (B) and (C) generally correspond to the indicated regions of interest (ROIs). **B)** Representative confocal micrograph projections (lateral view) show signal from UTRNCH::GFP expressed in the seam and signal from AJM-1::mCHERRY, which marks apical seam-hyp7 junctions. (Left) In merge, UTRNCH::GFP is false colored in magenta and AJM-1::mCHERRY in green. Dashed lines indicate the longitudinal cables of F-actin within the seam syncytium as detected 3 hours into the L4 stage and in the L4/Adult molt, respectively; arrows point to longitudinal cables of F-actin at the margins of the fused seam in mid L4; arrowheads mark jagged F-actin structures at the seam/hyp7 boundary. s=seam. **C)** Confocal micrograph projections show F-actin labeled by UTRNCH::GFP (false colored magenta in merge) expressed in the syncytial seam and AJM-1::mCHERRY (false colored green in merge), in animals undergoing the L4 to adult molt. Images were acquired using a Zeiss LSM880 with Airyscan processing. Yellow dashed lines indicate the two longitudinal cables of F-actin within the seam (detected in control); arrowheads point to small breaks in these cables in *nmy-1(RNAi)* animals. In *nmy-2(ne3409)* single and *nmy-1(RNAi); nmy-2(ne3409)* double mutants, internal longitudinal cables of F-actin were not detected, and the seam appeared distended. Jagged F-actin structures at the seam/hyp7

margins were readily detectable in all conditions (chevrons). **B-C)** Strains imaged were ARF404 and ARF410. Scale bar = 5μm.

Figure 5. F-actin dynamics in lateral hyp7. A) Representative confocal fluorescence projections from over 130 carefully staged individuals isolated from synchronized populations show F-actin labeled by UTRNCH::dsRED and detected at the apical cortex of hyp7 in worms developing from L4 to the adult stage. Arrowheads point to F-actin at margins adjoining the syncytial seam; chevrons point to margins with dim signal; arrows point to circumferential actin filament bundles (CFBs); and circles mark puncta. (Lower right) Digitally-brightened ROI shows CFBs in the portion of hyp7 overlying body wall muscles (2X exposure). **B)** Plot shows the intensity of F-actin signals at hyp7 margins detected at each stage. **C)** Plot shows the anisotropy of F-actin signals in the lateral region of hyp7. **D)** Confocal projections show fluorescence from hyp7>UTRNCH::dsRED, as in **(A)**. **E)** Intensity of F-actin signals at hyp7 margins detected in molting worms of each genotype, as in **(B)**. **F)** Anisotropy of F-actin signals detected in molting worms of each genotype, as in **(C)**. **B-C, E-F)** Lines and error bars represent the mean and interquartile range. ****P<0.0001, **P<0.01, $^{n.s.}$P>0.9 in **(C)** and $^{n.s.}$P>0.05 in **(F)**, Ordinary one-way ANOVA with Tukey's test for multiple comparisons. Margin intensity and anisotropy values represent 4 and 6 ROIs per worm assayed, respectively; N=3-7 per stage or condition. **A, D)** Strains imaged were ARF385 and ARF388. Scale bar = 10μm.

Figure 6. Changes in tissue ultrastructure coupled to morphogenesis of the alae. A) Transverse TEM micrographs of the lateral epidermis of wild-type L4 larvae captured at 25,000X. At left, early L4 approximately two to three hours into the L4 stage; on right, mid L4 approximately four to six hours into the L4 stage. Arrow points to nascent sheath; arrowheads indicate lateral outline of seam syncytium; s=seam, h7=hyp7, aj= apical junctions of seam and hyp7. Brackets show width of seam apical cortex at each stage. Adapted with permission from Singh & Sulston (1978) (Singh and Sulston, 1978). **B)** TEM micrographs of transverse sections through the seam and adjacent hyp7 syncytia show deformation in the apical surface of the epidermis and progressive deposition of the alae over the course of the L4/Adult molt. Brackets indicate the remnant of the pre-existing L4 cuticle; black arrowheads point to nascent adult cuticle; black arrows point to putative sheath between the L4 and adult cuticles. Chevrons point to secretory granules in the seam (i-ii). **C)** Transverse TEM section through the alae and underlying seam and hyp7 syncytia in a young adult. Anatomical illustration depicts hyp7, the syncytial seam, and overlying ridges of the adult cuticle in the same location and orientation as the micrographs shown (ROI depicted). **B-C)** Scale bar = 500nm.

Figure 7. Actin is required to pattern the sheath, which in turn patterns the adult alae. A) Representative confocal fluorescence projections show FL-FBN-1::mCHERRY, a component of the interim matrix or sheath, in animals undergoing the L4/Adult molt. **B)** Representative confocal fluorescence projections show signal from NOAH-1::GFP, another component of the sheath, in young adult animals freshly emerged from the L4/Adult molt. **A-B)** The approximate region above the seam syncytium is marked by a bracket. Panels on the right correspond to enlarged regions of interest demarcated by dashed boxes. In control, longitudinal sheath structures are indicated by yellow dashed lines. Corresponding features at the surface of the animal are marked by black dashed lines in DIC micrographs. In attenuated *actin(RNAi)* conditions, color-coded arrowheads point to specific features in regions of mazes in GFP or CHERRY (yellow), DIC (black), and overlay (white). In control and acute *actin(RNAi)* conditions, vertical arrows point to fluorescent signal in circumferential bands corseting the body. In overlay with DIC, fluorescent signal was false-colored in yellow. Images were acquired using a Zeiss LSM880 with Airyscan processing. **C)** DIC micrographs show the lateral surface of young adults. Brackets demarcate the region overlying the seam syncytium. In wild type, yellow and black dots mark the furrows and ridges of the alae along the A-P axis of the body, respectively (as in Fig. 2A and 3A). An arrow points to an instance of mazes. **A-C)** Strains imaged were ARF379, ARF415, and N2. Scale bar = 5μm. **D)** Graph shows the frequency of alae phenotypes in young adults of indicated genotypes. As above, each animal observed was binned in a single

category, with mazes given priority over other alae defects. Values represent the weighted average of two independent trials. Outcomes were classified as superficially normal vs. abnormal alae to perform Fisher's exact test, ****P<0.0001.

Figure 8. Model for morphogenesis of the adult integument via anisotropic apical constriction of the epidermis coupled to deposition of interim and permanent matrices. A) Graphical representation of the lateral surface of the seam and hyp7 syncytia, from seam fusion until adulthood. Rearrangements in the actin cytoskeleton in the tissue are depicted in red. Inward facing arrows in (2) represent apical constriction and related forces driving the narrowing of the apical seam cortex on the A-P axis. Outward facing arrows in (3) represent the gradual relaxation of the cell shape changes depicted above. **B)** Transverse cross-section of the seam, hyp7, and overlying extracellular matrices during apical constriction (A:1-2) and relaxation (A:3-4).

SUPPLEMENTAL MATERIALS

Supplemental Figure 1. Actin cytoskeletal architecture in the seam prior to maturation. Representative confocal micrograph projections (lateral view) show signal from UTRNCH::GFP expressed in the seam and signal from AJM-1::mCHERRY, which marks apical seam-hyp7 junctions. (Left) In merge, UTRNCH::GFP is false colored in magenta and AJM-1::mCHERRY in green. Seam cells undergo final asymmetrical cell division prior to maturation and associated homotypic fusion. Bracket marks region previously occupied by anterior daughter cell, which fused with hyp7; arrowhead marks boundary between posterior daughter cells before completion of homotypic fusion. s=seam; a=anterior, and p=posterior daughter cells. Strain imaged was ARF404. Scale bar = 5μm.

Supplemental Figure 2. CFBs interdigitate with hemidesmosomes and extend over the lateral epidermis during molts. A) Confocal micrograph projections showing fluorescence from hyp7>UTRNCH::dsRED (magenta in merge) and MUP-4::GFP (green in merge), an unconventional ECM receptor associated with the apical plaques of hemidesmosome, at 6hrs into the L4 stage. Dashed line marks boundary in hyp7 between regions overlying the pseudocoelom (lh7) and body wall muscles (mh7); arrow points to circumferential F-actin bundle continuous between hyp7 regions; s= seam. **B)** Merged confocal micrograph projections show intercalated stripes of UTRNCH::dsRED in hyp7 (magenta) and MUP-4::GFP (green) at indicated developmental stages. **C)** Confocal micrographs of a young adult show fluorescence from UTRNCH::dsRED and VAB-10A::GFP, which is a core component of hemidesmosomes, detected in hyp7 overlying the body wall muscle. (Bottom) Linescan along horizontal axis generated from the merged image. These particular images were acquired using a Zeiss LSM 880 with linear unmixing of dsRED and GFP signals. **A-C)** Strains imaged were ARF412 and ARF407. Scale bar = 5μm.

Supplemental Figure 3. Actin and apical ECM dynamics across the L2d-to-dauer transition. A) Confocal micrograph projections show F-actin labelled by UTRNCH::GFP in the seam cells of *daf-2(e1370)* larvae becoming dauers. Early in the molt, both axial and transverse F-actin cables (dashed lines and arrowheads) were detected near the cortex of relatively wide seam cells. Late in the L2d/Dauer molt, orthogonal F-actin structures (chevrons) were detected at the margins of thin (constricted) seam cells. **B)** Confocal micrograph projection shows FL-FBN-1::mCHERRY in a *daf-2(e1370)* mutant molting from L2d to dauer. Dashed lines indicate four longitudinal bands FL-FBN-1::mCHERRY thought to correspond to outer furrows of the nascent dauer alae; arrow points to circumferential band of FL-FBN-1::mCHERRY. **C)** Fluorescence and compound micrographs of an *aaaEx78[fl-fbn-1::mCherry]* dauer larva. Bracket demarcates width of dauer alae in DIC micrograph captured at the same depth of field as top panel. Lack of signal on the surface is consistent with temporary nature of the sheath, which is partly consumed and partly shed with the L2 cuticle. FL-FBN-1::mCHERRY is not

detected at the surface of the animal. (Bottom) Trace of dauer alae as detected in published transverse TEM micrographs shows typical four ridges and five furrows. **A-C)** Strains imaged were ARF416, ARF417, and ARF321. Scale bar = 5μm.

Supplemental Table 1: *C. elegans* strains used in this study.
Supplemental Table 2: Oligonucleotides used in this study.

REFERENCES

Aguinaldo, A.M., J.M. Turbeville, L.S. Linford, M.C. Rivera, J.R. Garey, R.A. Raff, and J.A. Lake. 1997. Evidence for a clade of nematodes, arthropods and other moulting animals. *Nature*. 387:489-493.

Ambros, V., and H.R. Horvitz. 1984. Heterochronic mutants of the nematode Caenorhabditis elegans. *Science*. 226:409-416.

Bosher, J.M., B.S. Hahn, R. Legouis, S. Sookhareea, R.M. Weimer, A. Gansmuller, A.D. Chisholm, A.M. Rose, J.L. Bessereau, and M. Labouesse. 2003. The Caenorhabditis elegans vab-10 spectraplakin isoforms protect the epidermis against internal and external forces. *The Journal of cell biology*. 161:757-768.

Boudaoud, A., A. Burian, D. Borowska-Wykret, M. Uyttewaal, R. Wrzalik, D. Kwiatkowska, and O. Hamant. 2014. FibrilTool, an ImageJ plug-in to quantify fibrillar structures in raw microscopy images. *Nature protocols*. 9:457-463.

Brenner, S. 1974. The genetics of Caenorhabditis elegans. *Genetics*. 77:71-94.

Burkel, B.M., G. von Dassow, and W.M. Bement. 2007. Versatile fluorescent probes for actin filaments based on the actin-binding domain of utrophin. *Cell motility and the cytoskeleton*. 64:822-832.

Cassada, R.C., and R.L. Russell. 1975. The dauerlarva, a post-embryonic developmental variant of the nematode Caenorhabditis elegans. *Dev Biol*. 46:326-342.

Costa, M., B.W. Draper, and J.R. Priess. 1997. The role of actin filaments in patterning the Caenorhabditis elegans cuticle. *Dev Biol*. 184:373-384.

Costa, M., W. Raich, C. Agbunag, B. Leung, J. Hardin, and J.R. Priess. 1998. A putative catenin-cadherin system mediates morphogenesis of the Caenorhabditis elegans embryo. *The Journal of cell biology*. 141:297-308.

Cox, G.N., M. Kusch, and R.S. Edgar. 1981a. Cuticle of Caenorhabditis elegans: its isolation and partial characterization. *The Journal of cell biology*. 90:7-17.

Cox, G.N., S. Staprans, and R.S. Edgar. 1981b. The cuticle of Caenorhabditis elegans. II. Stage-specific changes in ultrastructure and protein composition during postembryonic development. *Dev Biol*. 86:456-470.

Cox, T.R., and J.T. Erler. 2011. Remodeling and homeostasis of the extracellular matrix: implications for fibrotic diseases and cancer. *Dis Model Mech*. 4:165-178.

Devuyst, O., E. Olinger, and L. Rampoldi. 2017. Uromodulin: from physiology to rare and complex kidney disorders. *Nat Rev Nephrol*. 13:525-544.

Essmann, C.L., M. Elmi, M. Shaw, G.M. Anand, V.M. Pawar, and M.A. Srinivasan. 2017. In-vivo high resolution AFM topographic imaging of Caenorhabditis elegans reveals previously unreported surface structures of cuticle mutants. *Nanomedicine*. 13:183-189.

Fabritius H., S.C., Raabe D., Nikolov S., Friák M., Neugebauer J. . 2011. Chitin in the Exoskeletons of Arthropoda: From Ancient Design to Novel Materials Science. *In* Topics in Geobiology. Vol. 34. Springer, Dordrecht.

Forman-Rubinsky, R., J.D. Cohen, and M.V. Sundaram. 2017. Lipocalins Are Required for Apical Extracellular Matrix Organization and Remodeling in Caenorhabditis elegans. *Genetics*. 207:625-642.

Frand, A.R., S. Russel, and G. Ruvkun. 2005. Functional genomic analysis of C. elegans molting. *PLoS Biol*. 3:e312.

Fraser, A.G., R.S. Kamath, P. Zipperlen, M. Martinez-Campos, M. Sohrmann, and J. Ahringer. 2000. Functional genomic analysis of C. elegans chromosome I by systematic RNA interference. *Nature*. 408:325-330.

Hannezo, E., B. Dong, P. Recho, J.F. Joanny, and S. Hayashi. 2015. Cortical instability drives periodic supracellular actin pattern formation in epithelial tubes. *Proceedings of the National Academy of Sciences of the United States of America*. 112:8620-8625.

Herman, M.A. 2006. Hermaphrodite cell-fate specification. *WormBook : the online review of C. elegans biology*:1-16.

Hong, L., T. Elbl, J. Ward, C. Franzini-Armstrong, K.K. Rybicka, B.K. Gatewood, D.L. Baillie, and E.A. Bucher. 2001. MUP-4 is a novel transmembrane protein with functions in epithelial cell adhesion in Caenorhabditis elegans. *The Journal of cell biology*. 154:403-414.

Hu, P.J. 2007. Dauer. *WormBook : the online review of C. elegans biology*:1-19.
Hubbard, E.J., and D. Greenstein. 2005. Introduction to the germ line. *WormBook : the online review of C. elegans biology*:1-4.
Jenkin, P.M., and H.E. Hinton. 1966. Apolysis in arthropod moulting cycles. *Nature*. 211:871.
Johnstone, I.L. 1994. The cuticle of the nematode Caenorhabditis elegans: a complex collagen structure. *Bioessays*. 16:171-178.
Johnstone, I.L., Y. Shafi, and J.D. Barry. 1992. Molecular analysis of mutations in the Caenorhabditis elegans collagen gene dpy-7. *Embo J*. 11:3857-3863.
Jovine, L., H. Qi, Z. Williams, E. Litscher, and P.M. Wassarman. 2002. The ZP domain is a conserved module for polymerization of extracellular proteins. *Nature cell biology*. 4:457-461.
Kamath, R.S., and J. Ahringer. 2003. Genome-wide RNAi screening in Caenorhabditis elegans. *Methods*. 30:313-321.
Kang, H., I. Bang, K.S. Jin, B. Lee, J. Lee, X. Shao, J.A. Heier, A.V. Kwiatkowski, W.J. Nelson, J. Hardin, W.I. Weis, and H.J. Choi. 2017. Structural and functional characterization of Caenorhabditis elegans alpha-catenin reveals constitutive binding to beta-catenin and F-actin. *The Journal of biological chemistry*. 292:7077-7086.
Katz, S.M.-N., H.; Chong, T.; Meli, V.; Frand, A. 2015. FBN-1 is an apical matrix protein essential for the integrity of epithelial organs under mechanical stress during larval development., International Worm Meeting.
Kim, H.Y., V.D. Varner, and C.M. Nelson. 2013. Apical constriction initiates new bud formation during monopodial branching of the embryonic chicken lung. *Development*. 140:3146-3155.
Knight, C.G., M.N. Patel, R.B. Azevedo, and A.M. Leroi. 2002. A novel mode of ecdysozoan growth in Caenorhabditis elegans. *Evol Dev*. 4:16-27.
Koh, K., and J.H. Rothman. 2001. ELT-5 and ELT-6 are required continuously to regulate epidermal seam cell differentiation and cell fusion in C. elegans. *Development*. 128:2867-2880.
Koppen, M., J.S. Simske, P.A. Sims, B.L. Firestein, D.H. Hall, A.D. Radice, C. Rongo, and J.D. Hardin. 2001. Cooperative regulation of AJM-1 controls junctional integrity in Caenorhabditis elegans epithelia. *Nature cell biology*. 3:983-991.
Legan, P.K., V.A. Lukashkina, R.J. Goodyear, A.N. Lukashkin, K. Verhoeven, G. Van Camp, I.J. Russell, and G.P. Richardson. 2005. A deafness mutation isolates a second role for the tectorial membrane in hearing. *Nat Neurosci*. 8:1035-1042.
Locke, M., and P. Huie. 1979. Apolysis and the turnover of plasma membrane plaques during cuticle formation in an insect. *Tissue Cell*. 11:277-291.
Lockwood, C., R. Zaidel-Bar, and J. Hardin. 2008. The C. elegans zonula occludens ortholog cooperates with the cadherin complex to recruit actin during morphogenesis. *Curr Biol*. 18:1333-1337.
Loveless, T., and J. Hardin. 2012. Cadherin complexity: recent insights into cadherin superfamily function in C. elegans. *Curr Opin Cell Biol*. 24:695-701.
Lu, P., V.M. Weaver, and Z. Werb. 2012. The extracellular matrix: a dynamic niche in cancer progression. *The Journal of cell biology*. 196:395-406.
MacQueen, A.J., J.J. Baggett, N. Perumov, R.A. Bauer, T. Januszewski, L. Schriefer, and J.A. Waddle. 2005. ACT-5 is an essential Caenorhabditis elegans actin required for intestinal microvilli formation. *Molecular biology of the cell*. 16:3247-3259.
Maiden, S.L., N. Harrison, J. Keegan, B. Cain, A.M. Lynch, J. Pettitt, and J. Hardin. 2013. Specific conserved C-terminal amino acids of Caenorhabditis elegans HMP-1/alpha-catenin modulate F-actin binding independently of vinculin. *The Journal of biological chemistry*. 288:5694-5706.
Martin, A.C., M. Gelbart, R. Fernandez-Gonzalez, M. Kaschube, and E.F. Wieschaus. 2010. Integration of contractile forces during tissue invagination. *The Journal of cell biology*. 188:735-749.
Martin, A.C., and B. Goldstein. 2014. Apical constriction: themes and variations on a cellular mechanism driving morphogenesis. *Development*. 141:1987-1998.

Masuya, H., K. Shimizu, H. Sezutsu, Y. Sakuraba, J. Nagano, A. Shimizu, N. Fujimoto, A. Kawai, I. Miura, H. Kaneda, K. Kobayashi, J. Ishijima, T. Maeda, Y. Gondo, T. Noda, S. Wakana, and T. Shiroishi. 2005. Enamelin (Enam) is essential for amelogenesis: ENU-induced mouse mutants as models for different clinical subtypes of human amelogenesis imperfecta (AI). *Hum Mol Genet*. 14:575-583.

McMahon, L., R. Legouis, J.L. Vonesch, and M. Labouesse. 2001. Assembly of C. elegans apical junctions involves positioning and compaction by LET-413 and protein aggregation by the MAGUK protein DLG-1. *Journal of cell science*. 114:2265-2277.

Meli, V.S., B. Osuna, G. Ruvkun, and A.R. Frand. 2010. MLT-10 defines a family of DUF644 and proline-rich repeat proteins involved in the molting cycle of Caenorhabditis elegans. *Molecular biology of the cell*. 21:1648-1661.

Mok, D.Z., P.W. Sternberg, and T. Inoue. 2015. Morphologically defined sub-stages of C. elegans vulval development in the fourth larval stage. *BMC Dev Biol*. 15:26.

Monsalve, G.C., C. Van Buskirk, and A.R. Frand. 2011. LIN-42/PERIOD controls cyclical and developmental progression of C. elegans molts. *Curr Biol*. 21:2033-2045.

Moores, C.A., and J. Kendrick-Jones. 2000. Biochemical characterisation of the actin-binding properties of utrophin. *Cell motility and the cytoskeleton*. 46:116-128.

Morrissey, M.A., D.P. Keeley, E.J. Hagedorn, S.T. McClatchey, Q. Chi, D.H. Hall, and D.R. Sherwood. 2014. B-LINK: a hemicentin, plakin, and integrin-dependent adhesion system that links tissues by connecting adjacent basement membranes. *Developmental cell*. 31:319-331.

Muller, U., and P.G. Barr-Gillespie. 2015. New treatment options for hearing loss. *Nat Rev Drug Discov*. 14:346-365.

Page, A.P., and I.L. Johnstone. 2007. The cuticle. *WormBook : the online review of C. elegans biology*:1-15.

Pasti, G., and M. Labouesse. 2014. Epithelial junctions, cytoskeleton, and polarity. *WormBook : the online review of C. elegans biology*:1-35.

Pettitt, J., E.A. Cox, I.D. Broadbent, A. Flett, and J. Hardin. 2003. The Caenorhabditis elegans p120 catenin homologue, JAC-1, modulates cadherin-catenin function during epidermal morphogenesis. *The Journal of cell biology*. 162:15-22.

Piekny, A.J., J.L. Johnson, G.D. Cham, and P.E. Mains. 2003. The Caenorhabditis elegans nonmuscle myosin genes nmy-1 and nmy-2 function as redundant components of the let-502/Rho-binding kinase and mel-11/myosin phosphatase pathway during embryonic morphogenesis. *Development*. 130:5695-5704.

Plaza, S., H. Chanut-Delalande, I. Fernandes, P.M. Wassarman, and F. Payre. 2010. From A to Z: apical structures and zona pellucida-domain proteins. *Trends Cell Biol*. 20:524-532.

Podbilewicz, B., and J.G. White. 1994. Cell fusions in the developing epithelial of C. elegans. *Dev Biol*. 161:408-424.

Priess, J.R., and D.I. Hirsh. 1986. Caenorhabditis elegans morphogenesis: the role of the cytoskeleton in elongation of the embryo. *Dev Biol*. 117:156-173.

Qadota, H., M. Inoue, T. Hikita, M. Koppen, J.D. Hardin, M. Amano, D.G. Moerman, and K. Kaibuchi. 2007. Establishment of a tissue-specific RNAi system in C. elegans. *Gene*. 400:166-173.

Sapio, M.R., M.A. Hilliard, M. Cermola, R. Favre, and P. Bazzicalupo. 2005. The Zona Pellucida domain containing proteins, CUT-1, CUT-3 and CUT-5, play essential roles in the development of the larval alae in Caenorhabditis elegans. *Dev Biol*. 282:231-245.

Sarov, M., J.I. Murray, K. Schanze, A. Pozniakovski, W. Niu, K. Angermann, S. Hasse, M. Rupprecht, E. Vinis, M. Tinney, E. Preston, A. Zinke, S. Enst, T. Teichgraber, J. Janette, K. Reis, S. Janosch, S. Schloissnig, R.K. Ejsmont, C. Slightam, X. Xu, S.K. Kim, V. Reinke, A.F. Stewart, M. Snyder, R.H. Waterston, and A.A. Hyman. 2012. A genome-scale resource for in vivo tag-based protein function exploration in C. elegans. *Cell*. 150:855-866.

Schindelin, J., I. Arganda-Carreras, E. Frise, V. Kaynig, M. Longair, T. Pietzsch, S. Preibisch, C. Rueden, S. Saalfeld, B. Schmid, J.Y. Tinevez, D.J. White, V. Hartenstein, K. Eliceiri, P. Tomancak, and A. Cardona. 2012. Fiji: an open-source platform for biological-image analysis. *Nature methods*. 9:676-682.

Schultz, R.D., and T.L. Gumienny. 2012. Visualization of Caenorhabditis elegans cuticular structures using the lipophilic vital dye DiI. *J Vis Exp*:e3362.
Singh, R.N., and J.E. Sulston. 1978. Some Observations on Molting in Caenorhabditis-Elegans. *Nematologica*. 24:63-&.
Steiner, F.A., K.L. Okihara, S.W. Hoogstrate, T. Sijen, and R.F. Ketting. 2009. RDE-1 slicer activity is required only for passenger-strand cleavage during RNAi in Caenorhabditis elegans. *Nat Struct Mol Biol*. 16:207-211.
Sulston, J.E., and H.R. Horvitz. 1977. Post-embryonic cell lineages of the nematode, Caenorhabditis elegans. *Dev Biol*. 56:110-156.
Timmons, L., D.L. Court, and A. Fire. 2001. Ingestion of bacterially expressed dsRNAs can produce specific and potent genetic interference in Caenorhabditis elegans. *Gene*. 263:103-112.
Truman, J.W. 1992. The eclosion hormone system of insects. *Prog Brain Res*. 92:361-374.
Vasquez, C.G., M. Tworoger, and A.C. Martin. 2014. Dynamic myosin phosphorylation regulates contractile pulses and tissue integrity during epithelial morphogenesis. *The Journal of cell biology*. 206:435-450.
White, J.G. 1988. 4 The Anatomy. *In* The Nematode *Caenorhabditis elegans*. Cold Spring Harbor Monograph Archive. 81-122.
Willis, J.H., E. Munro, R. Lyczak, and B. Bowerman. 2006. Conditional dominant mutations in the Caenorhabditis elegans gene act-2 identify cytoplasmic and muscle roles for a redundant actin isoform. *Molecular biology of the cell*. 17:1051-1064.
Wu, S.K., and A.S. Yap. 2013. Patterns in space: coordinating adhesion and actomyosin contractility at E-cadherin junctions. *Cell Commun Adhes*. 20:201-212.
Yochem, J., T. Gu, and M. Han. 1998. A new marker for mosaic analysis in Caenorhabditis elegans indicates a fusion between hyp6 and hyp7, two major components of the hypodermis. *Genetics*. 149:1323-1334.

Figure 1

Katz and Frand (2017)

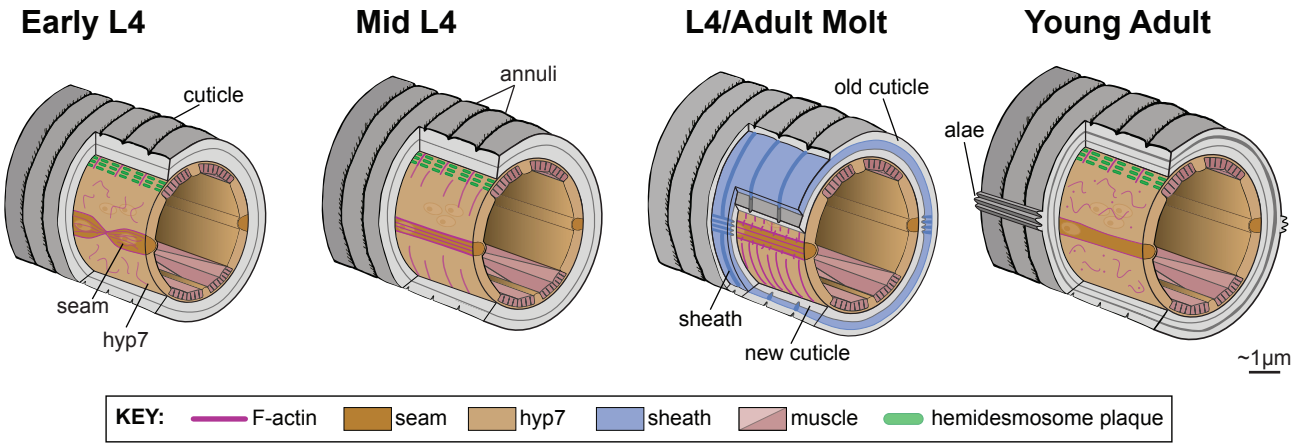

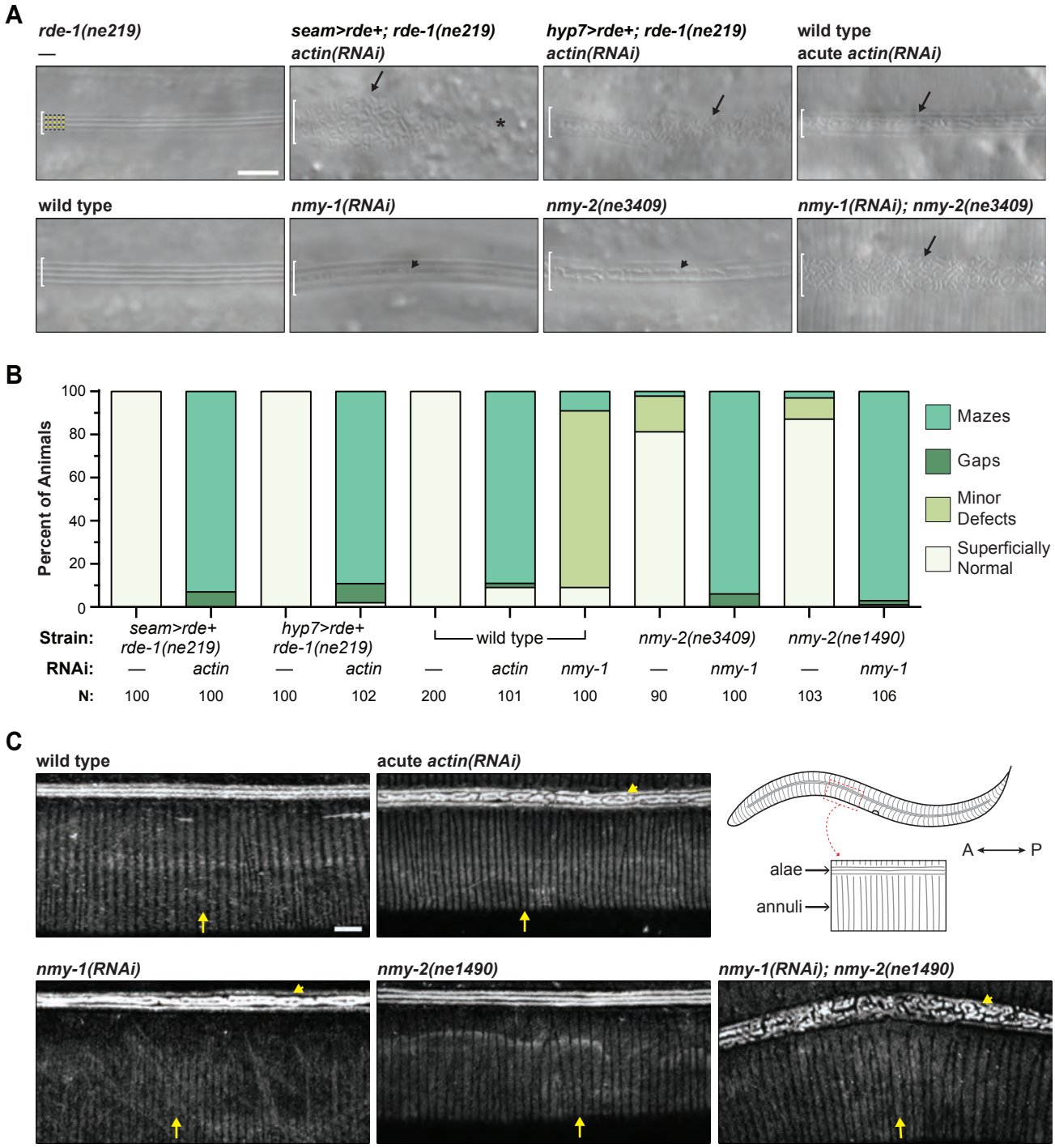
A
rde-1(ne219)
—
seam>rde+; rde-1(ne219)
actin(RNAi)
hyp7>rde+; rde-1(ne219)
actin(RNAi)
wild type
acute actin(RNAi)
wild type
nmy-1(RNAi)
nmy-2(ne3409)
nmy-1(RNAi); nmy-2(ne3409)
B
Percent of Animals
100
80
60
40
20
0
Mazes
Gaps
Minor Defects
Superficially Normal
Strain:
seam>rde+ rde-1(ne219)
hyp7>rde+ rde-1(ne219)
wild type
nmy-2(ne3409)
nmy-2(ne1490)
RNAi:
— actin — actin — actin nmy-1 — nmy-1 — nmy-1
N:
100 100 100 102 200 101 100 90 100 103 106
C
wild type
acute actin(RNAi)
A P
alae
annuli
nmy-1(RNAi)
nmy-2(ne1490)
nmy-1(RNAi); nmy-2(ne1490)

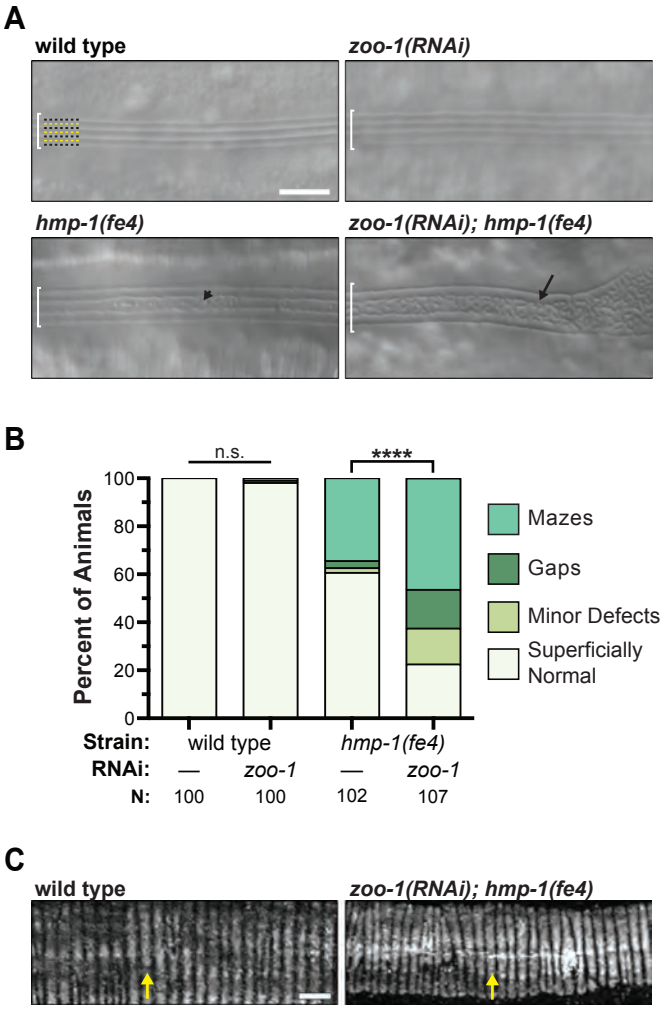
A
wild type
zoo-1(RNAi)
hmp-1(fe4)
zoo-1(RNAi); hmp-1(fe4)
B
n.s.
****
Percent of Animals
100
80
60
40
20
0
Mazes
Gaps
Minor Defects
Superficially Normal
Strain: wild type hmp-1(fe4)
RNAi: — zoo-1 — zoo-1
N: 100 100 102 107
C
wild type
zoo-1(RNAi); hmp-1(fe4)

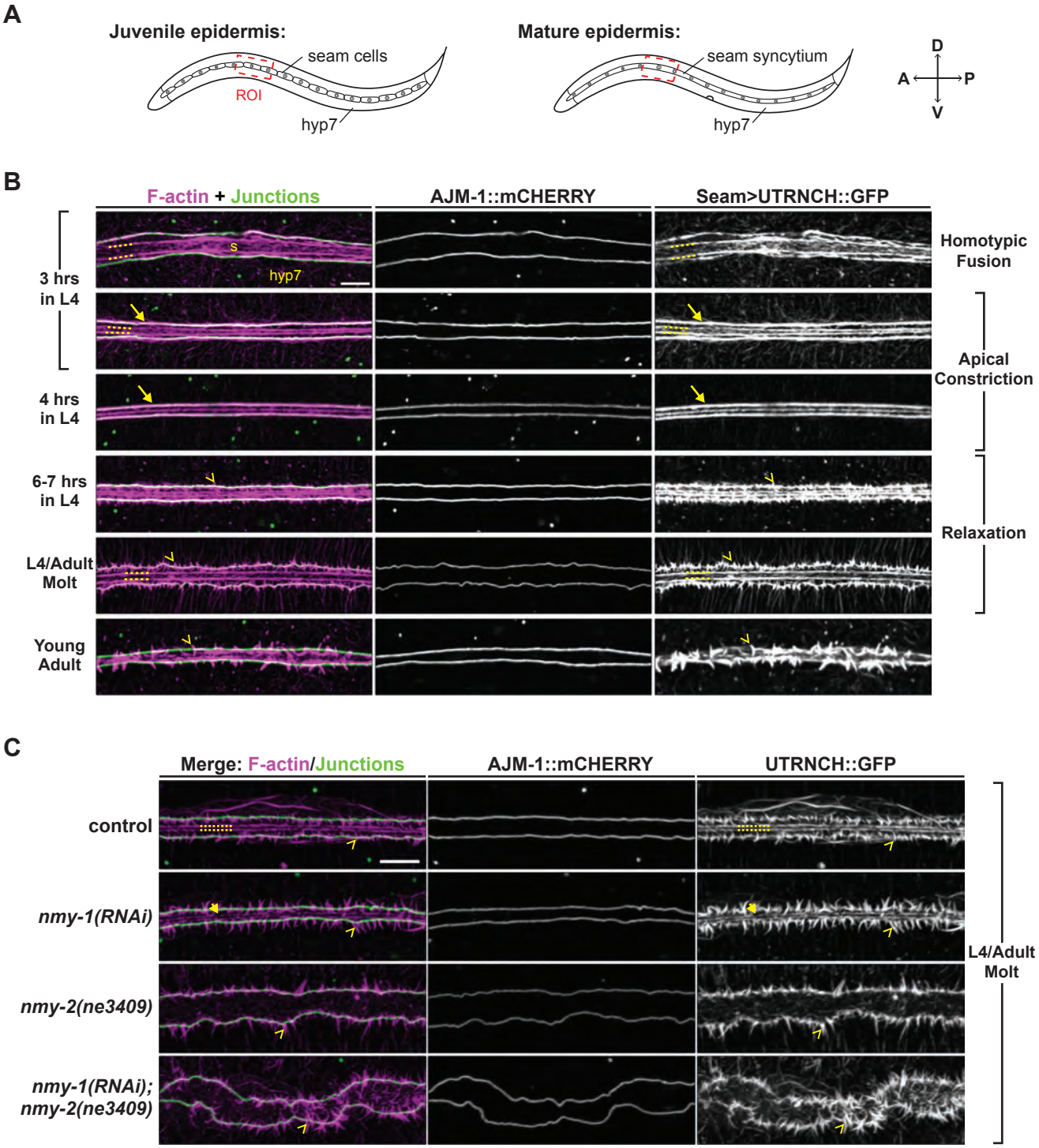
A
Juvenile epidermis:
seam cells
ROI
hyp7
Mature epidermis:
seam syncytium
hyp7
D
A
P
V
B
F-actin + Junctions
AJM-1::mCHERRY
Seam>UTRNCH::GFP
3 hrs in L4
4 hrs in L4
6-7 hrs in L4
L4/Adult Molt
Young Adult
s
hyp7
Homotypic Fusion
Apical Constriction
Relaxation
C
Merge: F-actin/Junctions
AJM-1::mCHERRY
UTRNCH::GFP
control
nmy-1(RNAi)
nmy-2(ne3409)
nmy-1(RNAi); nmy-2(ne3409)
L4/Adult Molt

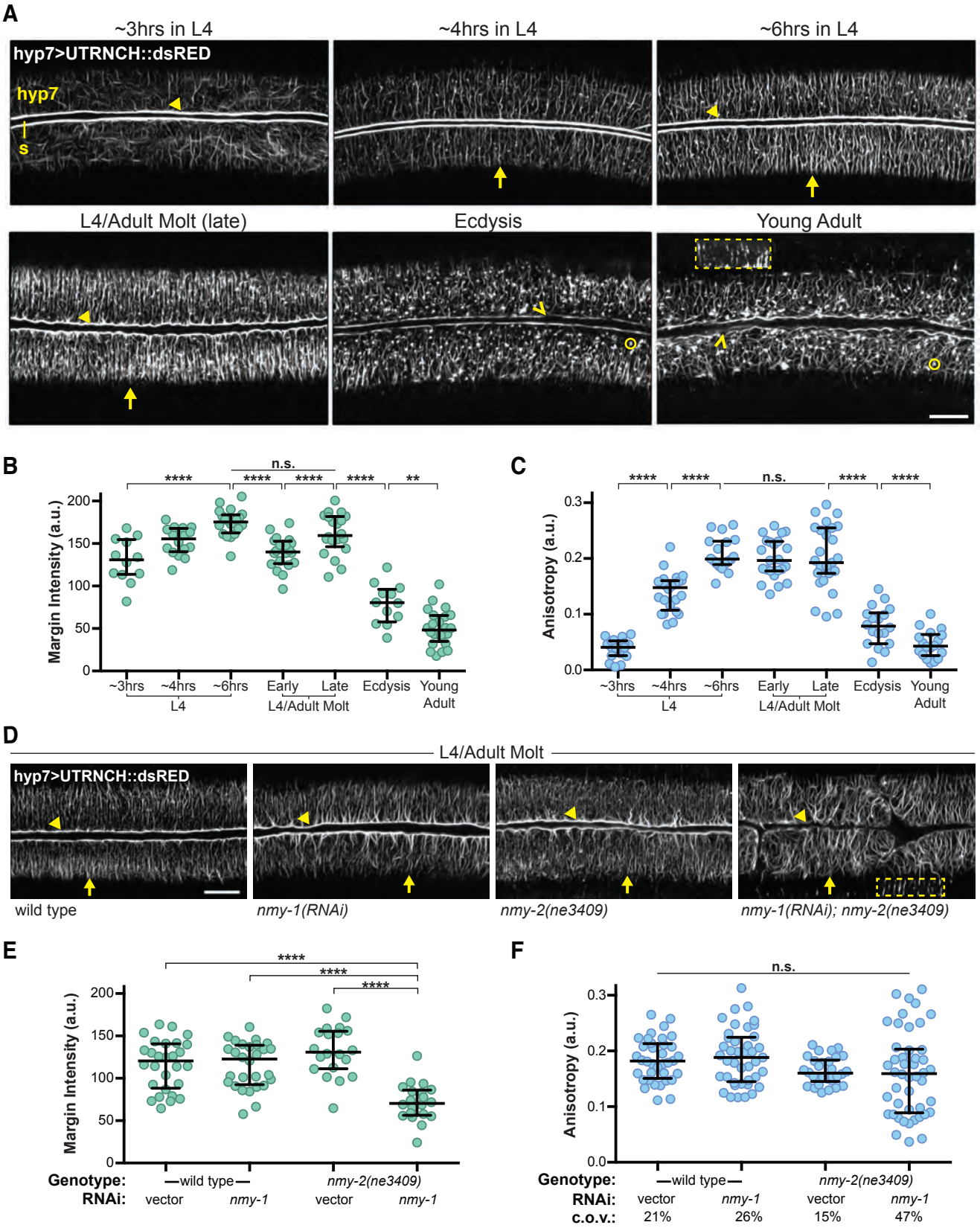
A
~3hrs in L4
~4hrs in L4
~6hrs in L4
hyp7>UTRNCH::dsRED
hyp7
s
L4/Adult Molt (late)
Ecdysis
Young Adult
B
Margin Intensity (a.u.)
n.s.
****
**
~3hrs
~4hrs
~6hrs
Early
Late
Ecdysis
Young Adult
L4
L4/Adult Molt
C
Anisotropy (a.u.)
n.s.
****
D
L4/Adult Molt
hyp7>UTRNCH::dsRED
wild type
nmy-1(RNAi)
nmy-2(ne3409)
nmy-1(RNAi); nmy-2(ne3409)
E
Margin Intensity (a.u.)
Genotype:
wild type
nmy-2(ne3409)
RNAi:
vector
nmy-1
vector
nmy-1
F
Anisotropy (a.u.)
n.s.
Genotype:
wild type
nmy-2(ne3409)
RNAi:
vector
nmy-1
vector
nmy-1
c.o.v.:
21%
26%
15%
47%

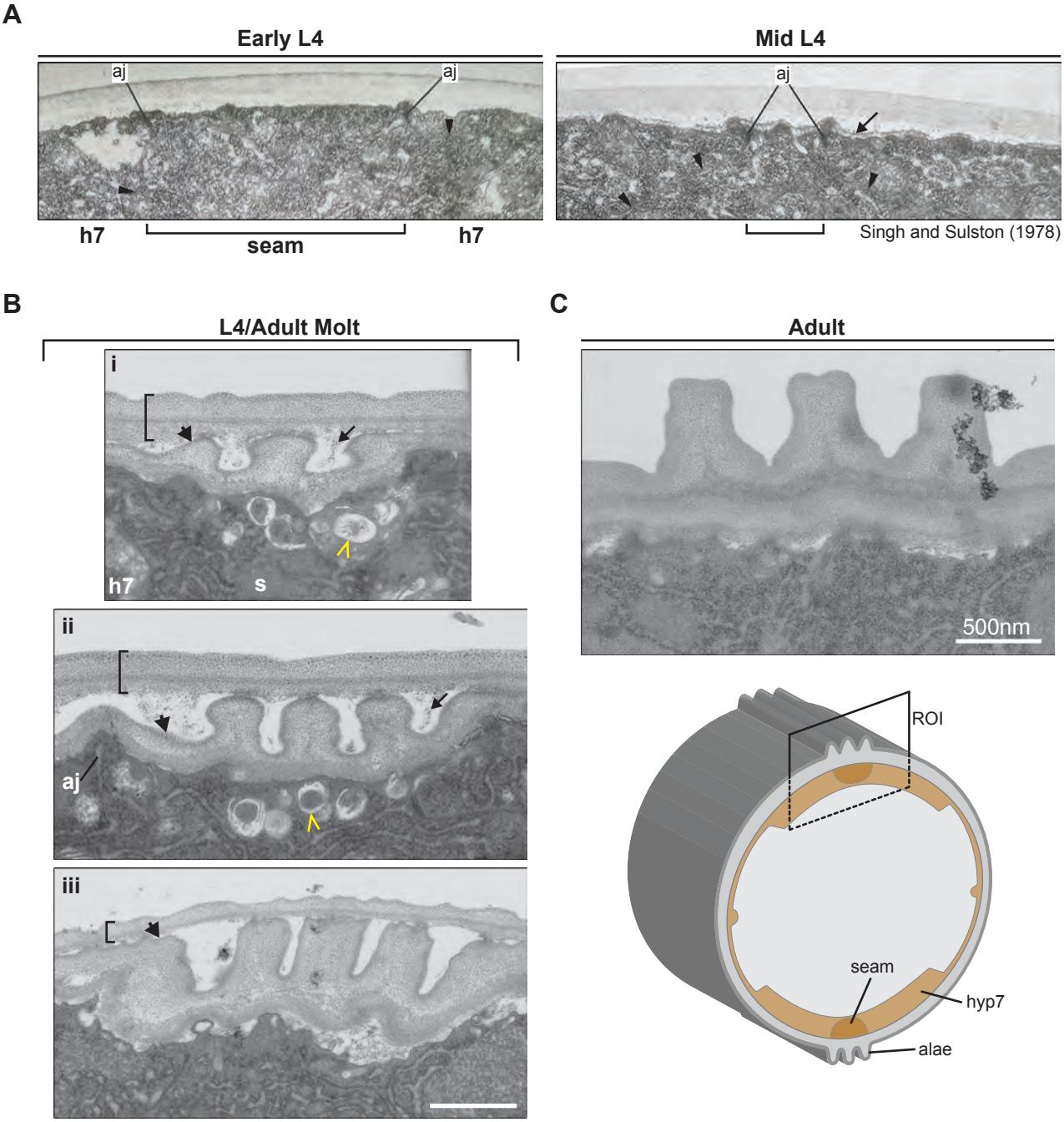
A
Early L4
aj
aj
h7
seam
h7
Mid L4
aj
Singh and Sulston (1978)
B
L4/Adult Molt
i
h7
s
ii
aj
iii
C
Adult
500nm
ROI
seam
hyp7
alae

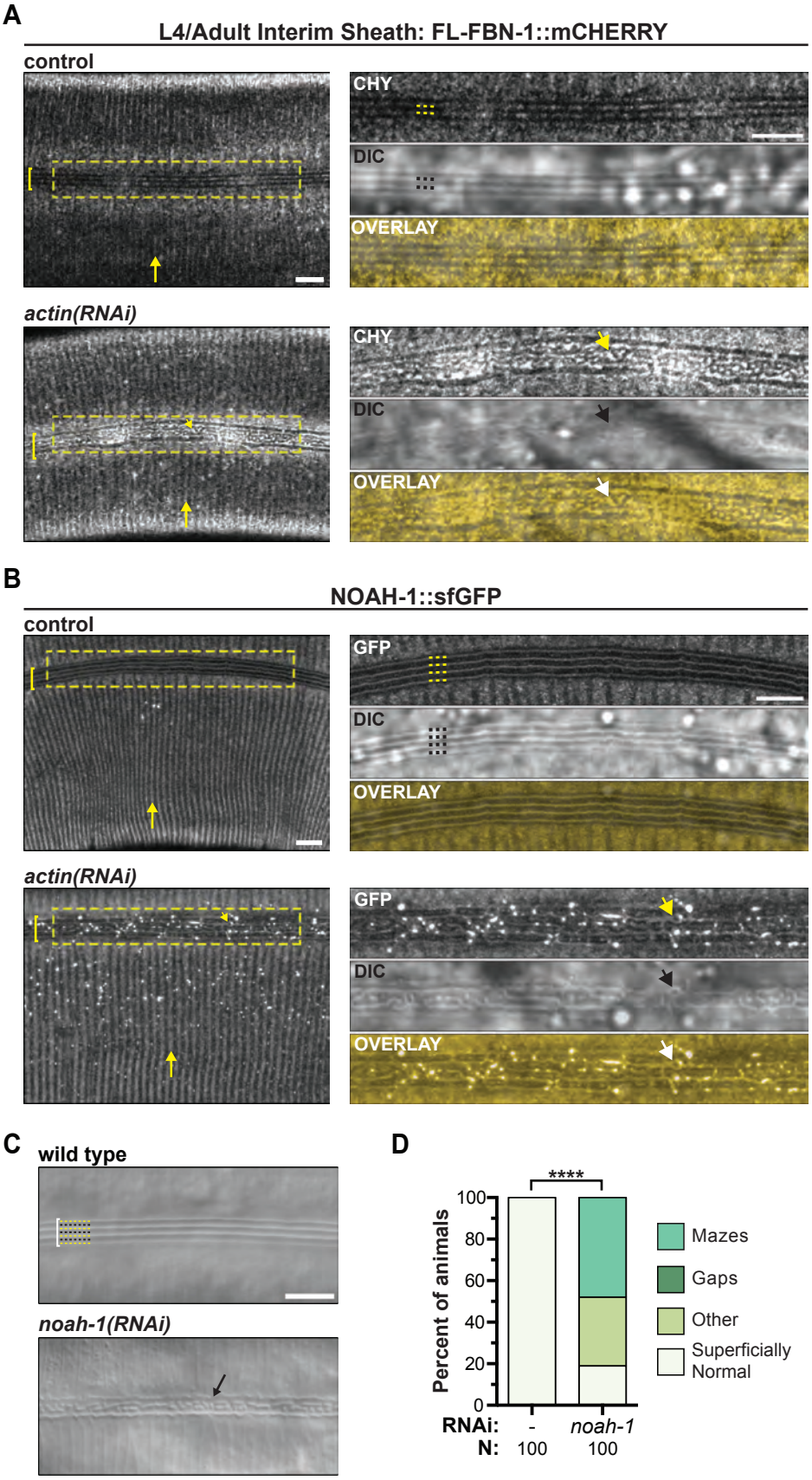
A
L4/Adult Interim Sheath: FL-FBN-1::mCHERRY
control
CHY
DIC
OVERLAY
actin(RNAi)
CHY
DIC
OVERLAY
B
NOAH-1::sfGFP
control
GFP
DIC
OVERLAY
actin(RNAi)
GFP
DIC
OVERLAY
C
wild type
noah-1(RNAi)
D
****
Percent of animals
100
80
60
40
20
0
RNAi:
N:
-
100
noah-1
100
Mazes
Gaps
Other
Superficially Normal

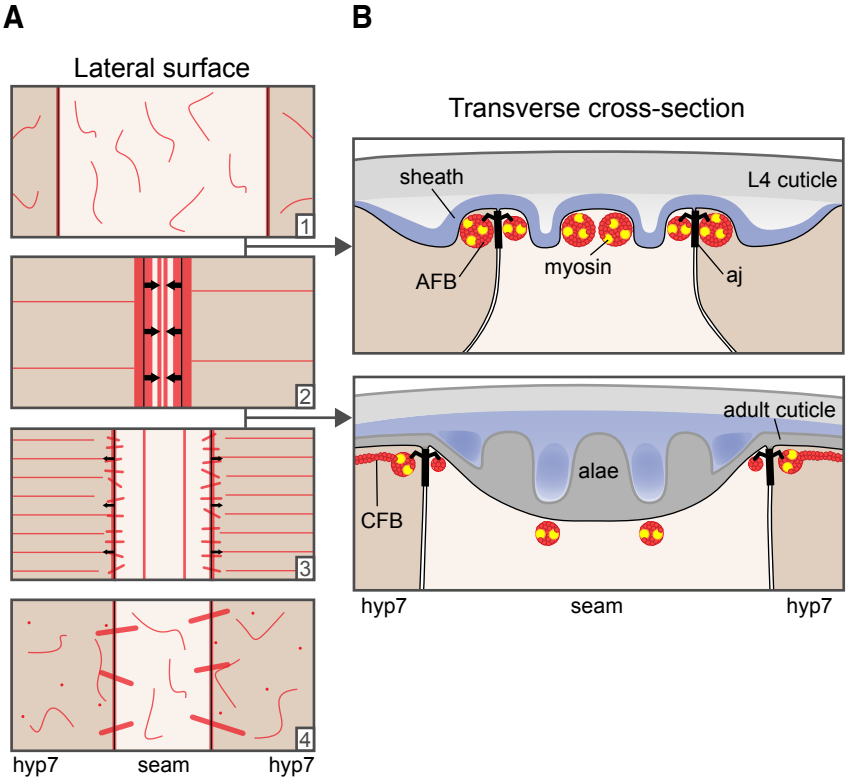
A
B
Lateral surface
Transverse cross-section
1
2
3
4
hyp7
seam
hyp7
sheath
L4 cuticle
AFB
myosin
aj
adult cuticle
alae
CFB
hyp7
seam
hyp7